



## Applications and limitations of constrained high-resolution peak fitting on low resolving power mass spectra from the ToF-ACSM

Hilkka Timonen<sup>1,\*</sup>, Mike Cubison<sup>2</sup>, Minna Aurela<sup>1</sup>, David Brus<sup>1</sup>, Heikki Lihavainen<sup>1</sup>, Risto Hillamo<sup>1</sup>, Manjula Canagaratna<sup>3</sup>, Bettina Nekat<sup>4</sup>, Rolf Weller<sup>3</sup>, Douglas Worsnop<sup>3</sup>, Sanna Saarikoski<sup>1</sup>

5 <sup>1</sup> Atmospheric composition research, Finnish Meteorological Institute, Helsinki, Finland

<sup>2</sup> TOFWERK AG, Thun, Switzerland

<sup>3</sup> Aerodyne Research Inc., Billerica, MA, USA

<sup>4</sup> Alfred-Wegner-Institut Helmholtz-Zentrum für Polar- und Meeresforschung, Bremerhaven, Germany

\*Correspondence to: H. Timonen (hilkka.timonen@fmi.fi)

10

**Abstract.** The applicability, methods and limitations of constrained peak-fitting on mass spectra of low mass resolving power ( $m/dm_{50} \sim 500$ ) recorded with a time-of-flight aerosol chemical speciation monitor (ToF-ACSM) are explored. Calibration measurements as well as ambient data are used to exemplify the methods that should be applied to maximise data quality and assess confidence in peak-fitting results. Sensitivity analyses and basic peak fit metrics such as normalised ion separation are employed to demonstrate which peak-fitting analyses commonly performed in high-resolution aerosol mass spectrometry are appropriate to perform on spectra of this resolving power. Information on aerosol sulphate, nitrate, sodium chloride, methanesulphonic acid as well as semi-volatile metal species retrieved from these methods is evaluated. The constants in a commonly used formula for the estimation of the mass concentration of hydrocarbon-like organic aerosol may be refined based on peak-fitting results. Finally, application of a recently-published parameterisation for the estimation of carbon oxidation state to ToF-ACSM spectra is validated for a range of organic standards and its use demonstrated for ambient urban data.

15

20



## 1. Introduction

Atmospheric aerosol influence health, climate and visibility (Pope and Dockery, 2006; IPCC 2013). All these influences are tightly linked with particulate matter (PM) concentration and PM chemical composition (IPCC 2013). Traditionally, aerosol composition was studied by collecting particulate matter on a filter substrate for an extended period ranging from hours to days and subsequent composition analysis in laboratory. Development of online analysis instruments, particularly based upon aerosol mass spectrometry, have enabled the measurement of chemical composition of PM in real time. The Aerodyne aerosol mass spectrometer (AMS; Jayne et al., 2000; DeCarlo et al., 2006) is designed to provide detailed information on size-resolved aerosol chemical composition for short to medium term campaigns (weeks to months); however it is not suitable for long-term monitoring without the presence of an operator. The Aerodyne aerosol chemical speciation monitor (Q-ACSM; Ng et al., 2011b) is based on AMS technology but adapted for long-term monitoring, however the quadrupole detector limits the mass resolving power to unity and provides reduced sensitivity compared with the AMS. A recently-developed version of this instrument employing time-of-flight (TOF) detection provides greater sensitivity and mass resolving power of around 500 (ToF-ACSM; Fröhlich et al., 2013). Whilst the increase in sensitivity relative to the Q-ACSM is an obvious advantage for measurements in clean locations such as Antarctica or for increasing temporal resolution, the limits of potential extra information afforded by the increased mass resolving power, and in particular the associated uncertainties on peak-fitting parameters, are as yet unexplored in the literature.

In analysis of high-resolution AMS data, peak-fitting is typically employed to retrieve signal intensities of ions whose peaks overlap in the mass spectrum, expanding greatly the content and quality of information that may be extracted from the data in comparison to simple peak integration (e.g. DeCarlo et al, 2006; Aiken et al, 2008). Fröhlich et al. (2013) demonstrated that peak-fitting could be applied to ToF-ACSM data and presented a simple example for a single isobaric peak, but the extent and limitations of the applicability of the technique were not explored. Recently, the uncertainty on fitted peak intensity associated with the constrained peak-fitting procedure employed by the AMS community has been explored and parameterisations for calculation of the precision reported (Corbin et al, 2015; Cubison and Jimenez, 2015). These are used, together with the appropriate sensitivity analyses, to assess the confidence in the peak-fitting results and draw conclusions on the appropriateness of applying peak-fitting for retrieval of overlapping ion peak intensities for a range of example scenarios.

## 2. Experimental

### 2.1. Time-of-flight aerosol chemical speciation monitor

The ToF-ACSM (Fröhlich et al., 2013; Aerodyne Research Inc., Billerica, USA) is designed for long-term monitoring of submicron aerosol composition with temporal resolution of typically 10 minutes (and up to 1 Hz) and mass resolving power  $m/\Delta m_{50}$  of typically 500 (and up to 600). Based on the sampling technology of the ToF-AMS (time-of-flight aerosol mass



spectrometer, Drewnick et al, 2005; DeCarlo et al, 2006), the ToF-ACSM contains a critical orifice to constrain the flow ( $1.4 \text{ cm}^3 \text{ s}^{-1}$ ) and an aerodynamic lens to focus submicron particles into a narrow beam introduced into a differentially-pumped vacuum chamber where the gas molecules tend to diverge from the beam path and are pumped away, concentrating the aerosol:gas molecule ratio by a factor of around  $10^7$ . The particle beam impacts a heated plate held at  $600^\circ\text{C}$  and the molecules are vapourised and immediately ionised using 70 eV electron impact ionisation. The ions are introduced into a compact time-of-flight mass analyser (ETOF, TOFWERK AG, Thun, Switzerland) and extracted orthogonally using pulsed extraction for eventual detection with a discrete dynode detector. Mass spectra are recorded with and without the use of a filter in the inlet line; the resulting difference in recorded signal is prescribed to the aerosol. These signals are converted to nitrate equivalent mass concentrations using the same ionisation efficiency calibration procedure utilised for the AMS and described by Jimenez et al. (2003). Post-processing was performed using the data analysis package “Tofware” (version 2.5.3, [www.tofwerk.com/tofware](http://www.tofwerk.com/tofware)) running in the Igor Pro (Wavemetrics, OR, USA) environment.

## 2.2. Measurement locations and datasets

Three ToF-ACSM datasets were used to study applicability and limitations of constrained peak-fitting on mass spectra recorded with the ToF-ACSM, measured in clean background conditions (Neumayer, Antarctica), in the urban background (SMEARIII) and in an industrial environment (underground mine).

### 2.2.1 Helsinki, Finland

ToF-ACSM measurements were conducted at the SMEARIII measurement station in Helsinki, Finland, from March 2 to March 8, 2014. The SMEAR III station ( $60^\circ 12'$ ,  $24^\circ 57'$ , 30 m.a.s.l., Järvi et al., 2009) is an urban background measurement station for the long-term measurement and investigation of chemical and physical properties of atmospheric aerosols and trace gases, meteorological parameters and turbulent fluxes. The station is situated on the Kumpula campus, 5 km northeast from the center of Helsinki. Approx. 200 m east of the station is a major road with heavy traffic (60 000 cars/day). During the measurement period presented here the PM concentrations (calculated using an assumed collection efficiency of 0.5) exhibited a mean average of  $16.2 \mu\text{g m}^{-3}$ . However, larger concentrations up to  $45 \mu\text{g m}^{-3}$  were observed (Fig. S1).

### 2.2.2 Antarctica

ToF-ACSM measurements were conducted at the Neumayer III station in Antarctica ( $70.6744^\circ \text{ S}$ ,  $8.2742^\circ \text{ W}$  [http://www.awi.de/en/go/air\\_chemistry\\_observatory](http://www.awi.de/en/go/air_chemistry_observatory); Weller et al., 2011) during the Antarctic summer from December 2014 to February 2015. Located far from primary emission sources, the Neumayer III station is an ideal location for conducting background measurements free from anthropogenic influences (Weller et al., 2015). The two most frequently-observed classes of aerosol observed in Antarctica contain sulphur and sea-salt. Sulphur-containing particles, whose secondary production in the atmosphere is controlled by pathways including photochemical reactions involving dimethyl sulphide (DMS) emitted by



the oceans, dominate particle number concentrations in the Antarctic atmosphere most of the time (Korhonen et al., 2008; Weller et al., 2011).

Very low background aerosol concentrations of less than  $1 \mu\text{g m}^{-3}$  were typically measured, consisting almost purely of sulphate and chloride compounds. Larger PM concentrations were observed during January and February (up to  $3 \mu\text{g m}^{-3}$ ) when the temperature was higher and the adjacent ocean ice-free. We have chosen two distinct episodes for use in analyses presented in this work. Each exhibited different characteristics and posed different problems for extracting information from the data using peak-fitting. Episode 1 (December 2-3, 2014) represents emissions from sea areas and had elevated chloride concentrations. During episode 2 (January 7-13, 2015) elevated sulphate and MSA concentrations were observed.

### 2.2.3 Underground mine

ToF-ACSM measurements were conducted at the Kemi Mine (Outokumpu Chrome Oy) 500 m below the surface during the spring of 2014 as a part of a project aiming to help development of a sustainable and safe mining environment. The main sources of particles in the underground mine were the ore extraction and processing for coarse particles and diesel exhausts from mining machinery and transport vehicles for submicron particles. A subset of data is used here in order to test peak-fitting on information-rich mass spectra taken in an environment with high PM concentrations.

## 3. Methods

### 3.1. Peak-fitting methodology

The post-processing software “Tofware” utilised for ToF-ACSM analysis uses a peak deconvolution routine where the peak positions are defined a priori and held fixed in the fitting procedure, based on the methodology utilised by the PIKA software of the ToF-AMS community (DeCarlo et al, 2006; Sueper, 2008). Electron impact (EI) ionisation, as is used in the ToF-ACSM, tends to ionise and fragment the molecules in a very consistent manner. Thus, one degree of freedom is removed from the ion fitting procedure, which can be based upon a comprehensive list of ions and their exact  $m/Q$  that define the fitted centroid values. Furthermore, the peak model (width and shape) is held fixed for a given isobaric mass and the mass calibration is also defined a priori and held constant. The only parameter to vary is thus peak intensity, for which the optimal values for all peaks at a given isobar are ascertained by non-negative least-squares optimisation using the active set method of Lawson and Hanson (1995). We present here a detailed description of each step in the setup of the peak-fitting routine, with exception of the mass calibration, which is discussed at length in the following section.



### 3.1.1. Mass spectral baseline subtraction

Mass spectra recorded using analogue-to-digital converters (ADC) to digitise the detector signal for data acquisition purposes, as is the case in the ToF-ACSM, can be expected to exhibit a non-zero mass spectral baseline as a result of background ions and, potentially, electronic noise (Fig. 1). In addition, peaks adjacent to large signals (such as  $N_2^+$  in the ToF-ACSM) can be expected to be superimposed upon a significant baseline varying in intensity with  $m/Q$ . It is important to subtract this baseline from the mass spectrum before carrying out the peak fit procedure, such that the assumed fixed peak model (width, shape) may be applied. As it is desired to let the analysis software execute peak-fitting as a batch process upon large numbers of mass spectra, a parameterisation is required which can reliably generate the MS baseline based on only a few tuneable parameters. ToFware achieves this through a simple two step process:

- i) A low-pass filter is applied to the MS to remove noise,
- ii) A running box average of the de-noised MS is generated based not on the mean but on the lowest data point in the box. Provided the box width is set large enough such that it extends over the entire width of a typical MS peak, step ii) effectively interpolates over the peaks as it takes the lowest data point at each step. Step i) has the effect of ensuring the calculated baseline tends to run through the centre and not along the bottom edge of the noise.

### 3.1.2. Determination of instrumental transfer function (peak model)

#### 3.1.2.1. Peak width

The width of an isolated ion peak is expected to observe a linear relationship with  $m/Q$ . A scatter plot of peak width vs.  $m/Q$  for isolated ions will thus highlight MS peaks that represent multiple, overlapping, ions as they will lie above the linear regression line (Meija and Caruso, 2004) as shown in Fig. 2. Junninen et al. (2010) and Stark et al. (2015) both used this effect to develop peak width parameterisations for use in atmospheric science analysis software; an adapted version of the method of Stark et al. is utilised here. Müller et al. (2013) report on a robust method for peak width calculation in proton mass-transfer mass spectrometry which utilises the same list of known isolated ions as the mass calibration. A similar method could certainly be employed for the lower part of the ToF-ACSM mass spectrum but would require extrapolation to high  $m/Q$ . To constrain the upper end of the linear regression, the following steps are taken:

- i) The  $N$  most intense peaks in the spectrum are found, where  $N$  is the largest  $m/Q$  measured divided by 3,
- ii) A single Gaussian fitted to each MS peak
- iii) A straight-line fit is applied to the scatter plot of FWHM vs  $m/Q$ ,
- iv) Step iii) is iterated, removing the point that lies the furthest above the fit line, until 10 peaks remain.

The user may choose additional peaks to use at step iv), and has the option to manually remove any points from the linear fit of step iii). Peak width is not expected to vary greatly over time other than with changes in instrument tuning. Thus the default peak width is calculated automatically for each 24-hr data file, but the user can define a revised version, typically once for each set of instrument tuning parameters during an experimental campaign, and save this in the data files for future use.



### 3.1.2.2. Peak shape

Owing foremost to the energetic primary ion beam, the measured shape of the ion peaks in the ToF-ACSM mass spectrum is often distinctly non-Gaussian and not easily described using mathematical functions. Therefore, rather than attempt to reduce the observed shape to a combination of functions, each peak is represented with a custom peak shape function following the high-resolution time-of-flight aerosol mass spectrometer (HR-ToF-AMS) methodology proposed by DeCarlo et al. (2006) and adapted for use in multiple atmospheric science analysis packages (Sueper, 2008; Junninen et al., 2010; Müller et al., 2013, Stark et al., 2015). The ToF-ACSM peak shape is determined using the following routine:

- i) The 20 largest peaks in the spectrum are found, and a single Gaussian fitted to each,
- ii) The measured shape of the peak is normalised to the fitted Gaussian width,
- iii) The second derivative of each normalised peak is analysed and peaks with shoulders are discarded,
- iv) All the remaining normalised shapes are averaged to generate the custom peak shape.

The user may additionally choose to fit more/fewer peaks at step i), and has the option to apply additional constraints such as monotonicity and thresholds on the min/max ion counts. The custom peak shape is typically defined once for each set of instrument tuning parameters during an experimental campaign and is saved in the data files for future use.

### 3.1.3. Peak list

For HR-ToF-AMS data, the list of ion peaks to be utilised during peak-fitting has been assembled and extended over a decade of instrument development and is quite comprehensive in nature (Sueper, 2008). Most of these ions are however unresolvable with the mass resolving power of the ETOF-equipped ToF-ACSM which precludes use of the HR-ToF-AMS ion list. The particular ions to fit must therefore be carefully considered based on targeted analyses, rather than taking the blanket approach of fitting everything as has been generally conducted for HR-ToF-AMS data. In the results section we present multiple case studies highlighting the state-of-the-art knowledge of which ions / ion groups are appropriate for inclusion in peak-fitting analyses of ToF-ACSM data.

## 3.2. Mass calibration

ToF-ACSM measurement profiles are typically converted from time-of-flight to mass-to-charge space and vice versa using the numerical relationship  $TOF = a + b \cdot \sqrt{m/Q}$ , where  $a$  and  $b$  are constants. In the constrained peak-fitting procedure employed during ToF-ACSM and AMS analysis, the accuracy and precision of the mass calibration are of critical importance, for the fitting is performed in time-of-flight space and the position of the fitted peaks held constant using fixed mass-to-charge values. In consequence, an imperfect mass calibration introduces imprecision in the fitted peak intensities, particularly for weaker signals in the presence of larger neighbours (Cubison and Jimenez, 2015), although imprecision in the fitted intensity is a significant source of error even for isolated peaks (Corbin et al., 2015). In practice, the precision of the mass calibration is



limited principally by i) the spectrometer resolving power, for wider calibrant peaks have a less well-defined centroid position, ii) counting statistics for the calibrant ions, and iii) non-ideally, the influence of neighbouring ions on assessment of calibrant peak position. Since i) is limited by the hardware, it may be considered an intrinsic limitation during data analysis and we will not consider it further. However, ii) and iii) are worth consideration as they can significantly degrade calibration accuracy. We note that Corbin et al. (2015) demonstrate that the AMS calibration can also contain biases that are of similar magnitude as the imprecision; consideration of their sources is however outside the scope of this paper. Finally, it is emphasised that this discussion pertains to fitted peaks and these effects would not introduce appreciable error in integrated isobaric peak intensities (processing of the full-resolution mass spectra to centroid, or “stick” spectra based on unit-mass resolution integration boundaries).

### 3.2.1. Effect of counting statistics

A significant source of calibration imprecision during monitoring operation can be counting error. In the lower mass range of the ToF-ACSM spectrum, several large signals arising from air and water ions (typically,  $\text{H}_2\text{O}^+$ ,  $\text{N}_2^+$ ,  $\text{O}_2^+$ , and  $\text{CO}_2^+$ ) may be used for mass calibration. Constraining the upper end is, however, significantly more challenging and is typically achieved by including the tungsten ions in the calibrant peak list. As the ToF-ACSM is usually operated at half the emission current of the AMS (to maximise filament lifetime), these are weak signals and subject to a significant level of noise from counting error. Unfortunately, the inclusion of even one weak ion in the mass calibration peak list greatly increases calibration imprecision (Cubison and Jimenez, 2015). A similar simulation of the mass calibration routine used in that study was employed here to assess the impact of the weak  $\text{W}^+$  signal on the ToF-ACSM mass calibration imprecision. Comparison of the  $\text{N}_2^+$  and  $\text{W}^+$  ion signals for several ambient ToF-ACSM datasets indicates a ratio  $\text{N}_2^+/\text{W}^+ \sim 50,000$ . Assuming a typical  $\text{N}_2^+$  signal of  $\sim 1\text{e}5$  ions/s, we expect total ion counts over an integration period of a half hour (typical averaging time for mass calibration) of  $\sim 2\text{e}8$  for  $\text{N}_2^+$  but only  $\sim 4\text{e}3$  for  $\text{W}^+$ . The noise in the tungsten signal leads to relative calibration precisions of  $\sim 2$  ppm for  $m/dm = 450$ . This value is however around an order of magnitude smaller than the biases in fitted position typically observed for the calibrant peaks (the difference in fitted peak position to that predicted from the calibration equation). It is nonetheless important that the spectra used for calibration are integrated over a sufficiently long period to ensure that imprecision arising from counting statistics is minimised.

### 3.2.2. Effect of isobaric ions

#### 3.2.2.1. Identifying influence of isobaric ions

Use of the tungsten ions for mass calibration in the ToF-ACSM is further complicated by potential interference from poorly separated isobaric ions. Fig. 3 compares ToF-ACSM data with higher-resolution data ( $m/dm_{50} \sim 10000$ ) that clearly shows the isobaric background organic ions (from electron impact ionisation of lab air) that contribute to the signal observed at the



tungsten peaks. The limited mass resolving power of the ToF-ACSM leads to single, broad peaks whose centroid values will be shifted to lower or higher  $m/Q$  according to the relative intensities of the various ions (Meija and Caruso, 2004).

5 However, it is still appropriate to utilise the tungsten peaks for mass calibration purposes if their signal is sufficiently large  
that the influence of the background peaks becomes negligible. Figure 4 compares lab data for clean and recently-vented, i.e.  
dirty, vacuum chambers. In the absence of significant background, as may be expected for ambient data in remote locations  
after a few days of pump-down, the tungsten ion signals are 1-2 orders of magnitude larger than the neighbouring peaks. This  
decreases for a recently-vented system to a factor of only 2-5 and with low filament emission currents can be expected to be  
even less. As the resolving power is not sufficient to unequivocally separate the tungsten ions from their neighbours, this leads  
10 to peak broadening and a centroid position that does not accurately reflect that of the tungsten ions (see e.g. Meija and Caruso,  
2004). Peak fits with freely-varying positions and intensities were applied to each of the four isobaric MS peaks where the  
tungsten isotopes can be measured (182, 183, 184 and 186 Th). The offsets of the fitted positions to the true tungsten isotopes  
were respectively -0.9, 0.6, 0.0 and -0.9 ppm in the clean case and -28, +152, -60 and -95 ppm in the recently-vented case. For  
peaks with mass resolving powers of  $\sim 500$ , fitted positional imprecisions of order a few ppm are to be expected. The offsets  
15 observed in the clean case are thus expected and use of the tungsten isotopes for mass calibration of datasets from clean  
locations can be considered justified. However, for datasets with significant background the offsets are larger than would be  
realistic were the peaks to truly represent isolated ions; their use as calibrant peaks could introduce bias and/or imprecision in  
the mass calibration of magnitude  $\sim 100$  ppm. The ToF-ACSM analysis software contains an integrated tool for assessing the  
degree to which offsets in the fitted positions of calibrant ions affect the mass calibration. Users are strongly encouraged to  
20 use this tool in order to evaluate whether individual ions with isobaric interferences can be effectively used for mass  
calibrations.

An additional check on whether a peak represents an isolated ion or not is easily performed by considering the peak width as  
a function of  $m/Q$ , which should follow a straight-line relationship (Meija and Caruso, 2004). In the ToF-ACSM, the many  
interferences across the MS lead to observed isobaric peak widths which usually broaden going to higher  $m/Q$ ; isolated ions  
25 at high  $m/Q$  stand out clearly as they lie under the trend, as is the case for tungsten in the clean-chamber MS in Fig. 4. In  
contrast, for the recently-vented chamber MS it is quite clear that the peak widths at 182, 184, 184 and 186 Th are broader  
than that which would be expected of isolated ions.

### 3.2.2.2. Compensating for influences of isobaric ions

Meija and Caruso (2004) show that, when the peak width is larger than the mass difference of two neighbouring peaks, the  
30 expected centroidal peak in  $m/Q$  is approximately the weighted average of the isobar masses (their Eq. 8):

$$m_{\text{observed}} \sim x * m_{\text{calibrant}} + (1-x) * m_{\text{influence}} \quad (\text{Eq. 1})$$



- where  $x$  is the relative abundance of the calibrant ion,  $m_{calibrant}$  the exact mass of the calibrant ion and  $m_{influence}$  the exact mass of an influencing peak. We propose that, in some cases, it may be justified to make a weighted adjustment of the mass positions of calibrant ions known to have influences from neighbouring, overlapping, peaks, based on the following assumptions:
- 5 i) all influencing isobaric peaks can be grouped together and considered as one single influencing peak in Eq. 1,
  - ii) the magnitude of the influencing peak is the same as the background peaks in the region of the MS where the calibrant ion is,
  - iii) the exact mass of the influencing peak takes the same mass excess =  $m/Q - \text{mod}(m/Q)$  as the background peaks in the region of the MS where the calibrant ion is.
- 10 Clearly any adjustment to calibrant ion exact masses introduces a bias into the peak-fitting procedure and, as will be discussed later, an analysis of the sensitivity of the fitted peak intensities to the mass calibration should be performed, where perturbations in the mass calibration are considered. However, the “best-case” scenario is that where the mass calibration reflects the user’s best estimate of the true mass positions of the peaks and thus, if it is known that the calibrant ion peaks are shifted due to
- 15 influencing, overlapping peaks, it may be argued that an attempt ought be made to correct for this, such that the sensitivity analysis starts from the best-estimated case.
- We illustrate this methodology using the tungsten isotope ions as an example. A single peak (using the true mass spectral peak shape but allowing the width to vary) is fitted to each isobaric peak in the MS between 160 and 200 Th, encompassing the mass positions of the tungsten ions. The mean average peak intensity and mass excess of the surrounding peaks are calculated. Peaks of this intensity and mass excess are used in eqn 1 to calculate the corresponding position of the tungsten (calibrant)
- 20 ions. Figure 5 exemplifies this approach. The surrounding isobaric peaks have an average mass excess of 0.095 Th and intensity of 665 ions (~15 times smaller than the tungsten peaks), leading to small positive shifts to the estimated “true” mass positions of the tungsten ions of ~ 0.006 Th (35 ppm).
- In this example, the compensation for the influencing peaks would be applied in the mass calibration by entering not the true tungsten isotope exact masses (red circles in Fig. 5) but rather these values less the 35 ppm offset calculated above (yellow
- 25 circles). To assess the validity of this method, the mass spectrum used in the example was recorded using a calibration gas SF<sub>6</sub> injected at the ioniser, giving rise to strong signals at the nominal masses 89, 108 and 127 Th from the ions SF<sub>3</sub><sup>+</sup>, SF<sub>4</sub><sup>+</sup> and SF<sub>5</sub><sup>+</sup> respectively. The mass calibration was performed based on the air peaks and the true or compensated tungsten peaks, and the mass offset of the SF<sub>3</sub><sup>+</sup>, SF<sub>4</sub><sup>+</sup> and SF<sub>5</sub><sup>+</sup> peaks calculated. As shown in Table 1, the mass accuracy was improved by ~ 20 ppm using the compensation technique described here.
- 30 For the example MS used in these calculations, the tungsten ion peaks were ~ 15 times stronger than the surrounding background peaks. Assuming the same background peaks were present, but exhibited different intensities relative to the



5 tungsten peaks, Figure 6 shows the estimated relative compensation that would be applied. For a  $W^+$  / background ratios of 100, a relative compensation of only 4 ppm is expected and this technique would have almost negligible effect on peak-fitting at the mass resolving power of the ToF-ACSM. However, for a  $W^+$  / background ratio of 5 (as may be expected in dirty environments), the relative compensation exceeds 100 ppm and use of the technique would need to be treated with the appropriate caution.

### 3.2.3. Alternative background peaks to tungsten ions

For datasets where the use of the tungsten ions in the mass calibration is not acceptable, an alternative constraint on the upper part of the MS is desired.

#### 3.2.3.1. Trichloroethylene

10 We propose that the fragmentation pattern from the industrial solvent Trichloroethylene is a potentially useful candidate for ToF-ACSM (and AMS) mass calibration. Isotope patterns matching the NIST electron impact reference MS for Trichloroethylene are apparent in multiple ToF-ACSM and AMS datasets. In particular, MS peaks which appear to correspond to the ions  $C_2^{35}Cl_3H^+$  and  $C_2^{37}Cl^{35}Cl_2H^+$  at the nominal masses 130 and 132 Th respectively are often visible in ToF-ACSM mass spectra recorded in clean locations with low background. The time-trend of the peak intensities for these ions follows  
15 that of the sensitivity of the instrument, indicating that the source of the interference lies within the vacuum chamber, most likely in the ionisation region. The peaks do not show up in the difference spectra and it is unlikely that Trichloroethylene gas molecules from an external source could sufficiently penetrate the differential pumping system, which dilutes background gas molecule concentrations by a factor of  $10^7$ .

The identification of the isotope pattern at 130, 132, and 134 Th as Trichloroethylene is supported by data from the HR-ToF-AMS. Figure 7 shows a HR-ToF-AMS MS recorded at the urban station in Helsinki (Mäkeläncatu) alongside a ToF-ACSM MS from the Neumayer station. Applying free-position peak fits as in section 3.2.2 gave fitted peak positions deviating from those of the Trichloroethylene ions of 0.2, -4.6 and 3.2 ppm respectively in the HR-ToF-AMS (limited by counting statistics) and 0.9, 4.9 and 109 ppm in the ToF-ACSM MS for 130, 132, and 134 Th. Whilst the Trichloroethylene ions are clearly well-separated from their neighbours by the HR-ToF-AMS, this is not the case for the ToF-ACSM and thus for calibration purposes  
25 the Trichloroethylene ion signals must, as was already pointed out for use of the tungsten ions, be significantly larger than the background in order to be considered as reliable mass calibration peaks. In the Neumayer dataset, the  $C_2^{35}Cl_3H^+$  and  $C_2^{37}Cl^{35}Cl_2H^+$  signals were roughly 30 times background. The influence of the background ions is thus small and a relative centroid position shift of only 4 ppm is observed. A compensation of the exact masses during calibration as described above would thus have negligible effect. The same is not true for the weaker  $C_2^{37}Cl_2^{35}ClH^+$  ion, whose centroid position is shifted  
30 relative to the stronger isotope peaks by over 100 ppm.



5

For the Neumayer data, Trichloroethylene proved to be a much more useful constraint on the upper region of the mass calibration than the tungsten ions, whose signal relative to background was relatively an order of magnitude weaker. Nonetheless, it is important to caveat that the peaks do not represent truly isolated ions, as is clearly visible comparing the HR-ToF-AMS and ToF-ACSM spectra in Fig. 7. Calibration biases of order a few ppm can be expected as a result, and should be considered when assessing peak-fitting results, as will be discussed later.

### 3.2.3.2. Extrapolation

10

In the absence of a valid constraint on the upper region of the mass calibration, the question is posed as to whether it is better to utilise the poorly-defined calibrant peak regardless, or simply extrapolate the calibration from the lower, well-defined, region of the MS. To investigate this, lab data was recorded where SF<sub>6</sub> gas was injected directly into the ionisation region, leading to strong signals at unit masses 89, 108 and 127 Th from the ions SF<sub>3</sub><sup>+</sup>, SF<sub>4</sub><sup>+</sup> and SF<sub>5</sub><sup>+</sup> respectively. A mass calibration was performed using the square-root relationship  $TOF = a + b \cdot \sqrt{m/Q}$  and the calibrant peaks OH<sup>+</sup>, N<sub>2</sub><sup>+</sup>, O<sub>2</sub><sup>+</sup>, Ar<sup>+</sup> and CO<sub>2</sub><sup>+</sup>. The offsets from the true peak positions for SF<sub>3</sub><sup>+</sup> and SF<sub>4</sub><sup>+</sup> were then assessed for the extrapolated calibration and again when additionally using SF<sub>5</sub><sup>+</sup> as a calibrant peak. For the constrained calibration (with SF<sub>5</sub><sup>+</sup>), offsets of -31 and 25 ppm were found for SF<sub>3</sub><sup>+</sup> and SF<sub>4</sub><sup>+</sup> respectively. Without the SF<sub>5</sub><sup>+</sup> constraint, these changed to -71 and -19 ppm respectively, a difference of up to approximately -40 ppm. In section 3.2.2 it was shown how interferences around the tungsten ions could lead to centroid peak position shifts of > 100 ppm, indicated that an extrapolated calibration could indeed be preferred over introduction of a bias of unknown direction and magnitude due to interferences at the calibrant peaks.

15

20

It is noted that the offsets (biases) of a few tens of ppm represent the limiting average mass accuracy across the MS range that may be expected during routine ToF-ACSM operation. Careful calibration selection, fitting of a sub-range and/or use of more complicated TOF/mass relationships may increase accuracy to below 10 ppm, but during normal operation the user should expect mass axis biases of around 10-20 and 50-100 ppm in the lower and upper regions of the MS respectively. Fitted peak intensities should be evaluated accordingly (see Corbin et al., 2015, for a detailed discussion on the influence of calibration bias on fitted peak intensity).

### 3.2.3.3. Addition of calibrant compounds

25

In the HR-ToF-AMS, the use of a plastic servo motor inside the vacuum chamber leads to a background peak at 149 Th from the ionisation of the phthalate molecules leaching out from the plastic. This is a useful and commonly-used calibrant peak that is however missing from the ToF-ACSM MS, as the instrument does not utilise this particular component. In the Q-ACSM, a naphthalene source is intentionally installed in the ioniser region to generate known background peaks for both transmission correction and mass calibration. In the interest of securing a decent calibration, installation in the vacuum chamber of a naphthalene source or a simple plastic element known to release phthalates into the environment could be a useful future modification to the instrument.

30



### 3.2.4. Evaluating calibration biases

In certain cases, a bias exists in the mass calibration fit residuals which takes an apparent polynomial shape in mass-to-charge space, as exemplified in Fig. 8. It is known that unusually long extraction pulse lengths can exacerbate the magnitude of these biases. The mass accuracies of the fit residuals are biases and, for a given instrumental tuning and timing setup, tend to be invariant over time. These biases have been shown to propagate into fitting errors (Corbin et al., 2015) and it is desired to compensate for them during mass calibration.

For the measurement in Fig. 8, the calibrant gas SF<sub>6</sub> was injected at the ioniser to provide a known set of strong calibrant peaks to exemplify this issue. Importantly, when the assumption is taken that the mass calibration biases are invariant with time, the polynomial fit to the residuals can be determined on a single MS and held fixed thereafter. A similar methodology has been employed to fix the exponent parameter in previous studies (DeCarlo et al., 2006). A MS with known calibrant ions in the central mass range exhibiting strong mass spectral peaks can thus be used to minimise the residuals, and this subtraction applied to all calibrations in the entire dataset time-series, which are in turn performed using the standard square-root fit only on stronger calibrant peaks such as N<sub>2</sub><sup>+</sup>, O<sub>2</sub><sup>+</sup> or CO<sub>2</sub><sup>+</sup>.

For routine ToF-ACSM analysis, where SF<sub>6</sub> fragment ions are not available, other calibrant ions would be required in the centre region of the MS to determine potential biases. The trichloroethylene, phthalate or naphthalene ions discussed above would be useful candidates. Indeed, in Fig. 8 the phthalate fragment ion at 149 Th is included in the calibrant peak list; the trichloroethylene peaks were, however, poorly defined owing to the much larger signal from the neighbouring SF<sub>5</sub><sup>+</sup> isotopes.

### 3.3 Peak-fitting uncertainties and terminology

Cubison and Jimenez (2015) give parameterisations to estimate the precision,  $\sigma_I$ , on fitted peak intensity for a system of two overlapping peaks using the same constrained peak-fitting procedure employed in this study. The two dependent parameters are the ratio of the two peak intensities,  $R_I$ , and the peak separation normalised to half-width at half-maximum (HWHM),  $X$ . As  $R_I$  increases, the precision with which the intensity of the less-intense ion peak can be fitted degrades. As  $X$  decreases, the same is true for both the more- and less-intense peaks. As a general rule, for  $R_I$  up to  $\sim 10$ , the fitted intensity of the child peak can be retrieved with acceptable precision for  $X$  as low as  $\sim 0.7$ . For smaller  $X$ , the imprecision increases and obtaining reliable results becomes challenging and eventually impossible. Peaks separated by  $X > 1.6$  can nearly always be reliably fitted, except in the case of  $R_I > 200$ , above which the imprecision on the fitted parameters of the less-intense peak is so great as to preclude their use in data analysis. We make use of this parameterisation in this study when discussing peak separations, which we state henceforth as  $X$ , i.e. normalised to HWHM.



## 4. Results and discussion

### 4.1. Ammonium

Data collected at the urban background station, SMEARIII, is used to study fitting of main inorganic ions, ammonium, nitrate and sulphate. Peak-fitting is routinely used on HR-ToF-AMS spectra to determine ammonium signal intensities, as  $\text{NH}_2^+$ ,  $\text{NH}_3^+$ , and  $\text{NH}_4^+$  all have large isobaric interferences (from  $\text{O}^+$ ,  $\text{HO}^+$  and  $\text{H}_2\text{O}^+$  respectively) and the integrated data time-series, constructed based on molecular fragmentation patterns which account for these large interferences (Allan et al., 2004), are thus noisy and detection limits correspondingly high. Fröhlich et al. (2013) applied peak-fitting to ToF-ACSM spectra and concluded that the  $\text{NH}_x$  ions were unresolvable from the interfering ions; we extend this discussion, with reference to the peak separations and expected intensity ratios, as the  $\text{NH}_x$  ions exemplify how the intensities of well separated peaks cannot always be accurately fitted. In the case of  $\text{NH}_2^+$ ,  $\text{NH}_3^+$ , and  $\text{NH}_4^+$ ,  $X$  approaches unity and the peaks can be considered partially separated. However, for peak ratios over 100 as are observed for these ions,  $X > 1$  is required even to achieve precisions on fitted intensity,  $\sigma_I$ , of 100% (Cubison and Jimenez, 2015), effectively precluding successful peak-fitting for all but the strongest ammonium signals. The only possibility for extracting useful information on ammonium from peak-fitting is thus at 15 Th where the interferences on  $\text{NH}^+$  are much smaller, as exemplified in Fig. 9. However, with peak separations to the neighbouring ions of  $X = 0.5$ , the imprecision expected in the fits is still large. Batch peak-fitting at 15 Th on ammonium nitrate calibration data yielded a time-series for  $\text{NH}^+$  whose signal:noise was similar to that of the integrated peak time-series. However, peak-fitting did not improve the quality of the data and thus for ammonium could only be used to help support assumptions required to construct the integrated data fragmentation table. It is estimated that mass resolving power approaching 1000 in this lower region of the MS would be required in order to reliably deconvolve the ammonium peak intensities.

### 4.2. Nitrate

In AMS analysis, concentrations of aerosol species from integrated unit mass data are calculated based on well described fragmentation patterns (Allan et al., 2004). Previous studies have shown that, in many ambient conditions, the default fragmentation patterns work well. However, in the case of high organic loadings and particularly during biomass-burning events, the assumptions tend to break down and nonsensical mass concentrations may result (e.g. Ortega et al., 2013). In general, it is preferred to construct the time-series from the sum of individual fitted ion intensities, providing of course that the uncertainty on these values is not large.

Inorganic nitrate is an important aerosol component whose principal contributing ion signals,  $\text{NO}^+$  and  $\text{NO}_2^+$ , both suffer from isobaric interferences due to neighbouring organic ions. Although Fröhlich et al. (2013) reported that it should be possible to use peak-fitting to resolve these interferences, the peak separations are very small indeed and no uncertainties or confidence metrics were presented. We address these issues here in detail.



At 30 Th the peak separations of  $\text{NO}^+$  from the organic isobaric interferences  $\text{CH}_2\text{O}^+$  and  $\text{C}_2\text{H}_6^+$  are  $X \sim 0.3$  and  $1.3$  respectively (Fig.10). A similar situation presents itself for  $\text{NO}_2^+$  at 46 Th (isobaric ions  $\text{CH}_2\text{O}_2^+$ ,  $\text{C}_2\text{H}_6\text{O}^+$ ). Calculating peak intensity via peak-fitting on fixed-position peaks separated by  $X \sim 0.3$  is extremely sensitive to the mass calibration. However, fortuitously in this case, the isobars 30 and 46 Th both lie close to calibrant ions used in the mass calibration; in the case of 30 Th the isobar is surrounded by  $\text{N}_2^+$  at 28 and  $\text{O}_2^+$  at 32 Th respectively. As a result, the bias expected in the calibration is very small relative to other regions in the mass spectrum (where the calibration may be extrapolated) and its magnitude can be predicted from the biases of the calibrant ions themselves.

Given the expected sensitivity of the highly-overlapping fits to the mass calibration, it is appropriate to conduct a sensitivity analysis to assess the degree of confidence that might be drawn from the fitted intensity values. Tofware offers a graphical tool for this purpose. An example is given for the isobar 30 Th, with fitted ions  $\text{NO}^+$ ,  $\text{CH}_2\text{O}^+$  and  $\text{C}_2\text{H}_6^+$ , in Fig. 11, using data from the SMEAR III campaign. Using the ions  $\text{H}_2\text{O}^+$ ,  $\text{N}_2^+$ ,  $\text{O}_2^+$  and  $\text{CO}_2^+$  to perform the mass calibration gave mass accuracies of between 2 and 13 ppm. Assessment of the sensitivity of the fitted intensities at 30 Th to mass calibration bias does not therefore need to consider much larger values than this; we conservatively chose 20 ppm, which equates to about 5% of the separation of the ions  $\text{NO}^+$  and  $\text{CH}_2\text{O}^+$ . In the general case, a larger perturbation value of between 50 and 100 ppm would be appropriate, depending on the confidence in the calibration.

From Fig. 11 one can take confidence that the fitted  $\text{NO}^+$  ion intensities are reliable. Firstly, consider the time-series of the fitted vs integrated peak intensities and their residuals for the un-perturbed mass calibration (left panels). The sum of the fitted peak intensities matches the integrated values to within a few percent. For 20-second averaging of a peak with a significant non-zero MS baseline and closely-separated neighbouring isobaric peaks (which influence the integrated intensities), this level of agreement is indeed indicative that the peak-fitting process has been properly performed. The step changes in the summed fitted intensity as the aerosol filter is switched in/out of the inlet line are also accurately captured.

The influence of perturbing the mass calibration is shown in the right panels as a time series (bottom) and scatter plot (top). When positively perturbing the calibration by 20 ppm (shifting the entire mass axis  $20 \text{ ppm} = 30 \text{ Th} * 20/1\text{e}6 = 0.0006 \text{ Th}$ , but holding peak positions fixed), the fitted  $\text{NO}^+$  intensity increases by 10 %. A negative perturbation of similar magnitude would decrease fitted intensity by 12 %. It is important to note that this is a sensitivity analysis and not an uncertainty calculation on the fitted intensities, nonetheless the method does offer a useful validity check on the fitted parameters. We henceforth refer to the relative intensity bias (offset, in %) introduced by calibration perturbation as  $\Delta_I$ .

Further to the perturbed time-series, the estimated precision on fitted intensity from the parameterisation of Cubison and Jimenez (2015),  $\sigma_I$ , is also shown on the un-perturbed intensity time-series (shaded area, bottom right panel). The fitted intensity of the  $\text{NO}^+$  ion is deconvolved with  $\sigma_I$  less than a few percent. Although this example presents a truly challenging peak-fitting scenario with limited signal and a large degree of peak overlap, one may draw conclusions based on the actual



fitted peak intensities provided they held true for changes of roughly +/- 10 %. Similar conclusions may also be drawn looking at  $\text{NO}_2^+$  at 46 Th (Fig. S2).

5 Finally, it is noted that, for the data shown, the organic mass loading was approx. 1.5 times that of the nitrate. In spectra with large organic signals, the relative strength of the nitrate ions to the organic interferences would be smaller and the corresponding uncertainty larger. Nonetheless, the same methodology presented here could be applied to assess the uncertainties.

### 4.3. Sulphate

10 Sulphate is a further important inorganic aerosol component measured by the ToF-ACSM. The principal contributing ions,  $\text{SO}^+$ ,  $\text{SO}_2^+$ ,  $\text{SO}_3^+$ ,  $\text{HSO}_3^+$  and  $\text{H}_2\text{SO}_4^+$ , are all affected by isobaric organic influences and the total sulphate concentration from integrated peak data over the nominal masses is, as per ammonium and nitrate, calculated based on assumed fragmentation patterns to account for these influences (henceforth referred to simply as “integrated data”). Like nitrate, these assumptions tend to break down for high organic mass loading and particularly for biomass-burning. However, with  $X$  values relative to the closest organic interferences of 0.5 - 0.8, constrained peak-fitting can be employed to directly calculate the sulphate ion signals with acceptable uncertainty. To demonstrate this, peak-fitting was performed on the SMEAR III dataset and an analogous sensitivity analysis was performed as presented for nitrate in the previous section (Figures S3-S7). The mass calibration perturbation employed for these sensitivity analyses reflected the position of the ions under study in the mass spectrum, relative to those used to perform the calibration ( $\text{H}_2\text{O}^+$ ,  $\text{N}_2^+$ ,  $\text{O}_2^+$  and  $\text{CO}_2^+$ ). Thus, the confidence in the mass calibration at 48 Th ( $\text{SO}^+$ ) is quite high and a 20 ppm perturbation was applied. In contrast at 98 Th ( $\text{H}_2\text{SO}_4^+$ ), the calibration is somewhat extrapolated and a 50 ppm perturbation was applied. The resulting sensitivities of the fitted intensities to calibration perturbations,  $\Delta I$ , ranged from approx. 3 to 30 %.

The SMEAR III data is used to demonstrate construction of a mass-loading time-series for sulphate based on the sum of the sulphate ion signals retrieved from peak-fitting (Fig. 12) The sum of the fitted intensities was able to reconstruct the same time-series as that from the fragmentation table with only 3% difference (integrated  $\sim 1.03$  \* fitted), demonstrating the validity of the method.

25 Figure 12 shows the fitted intensities of the isobaric interferences from organic ions. The ratio of the organic signal from the integrated data to the sum of the fitted intensities of the organic ions is  $0.64 \pm 0.40$ . Overall, the peak-fitting method weighted the allocation of the ion signals more heavily towards organic than the fragmentation table approach. However, the differences are small and the only significant conclusion that may be drawn is that, for this dataset, the methods are consistent to within a few percent.



#### 4.4. Sodium Chloride

The Neumayer station, situated in a clean environment adjacent to the open ocean, provides an ideal location to study compounds originating from the sea. Data collected on Neumayer station was used to study peak-fitting of sodium, chloride and methanesulphonic acid. The mass calibration for the Neumayer dataset was performed using the following calibrant ions;  $\text{H}_2\text{O}^+$ ,  $\text{N}_2^+$ ,  $\text{O}_2^+$ ,  $\text{Ar}^+$ ,  $\text{CO}_2^+$ ,  $\text{SO}_2^+$ ,  $\text{C}_2^{35}\text{Cl}_3\text{H}^+$ ,  $\text{C}_2^{35}\text{Cl}_2^{37}\text{ClH}^+$ . The isolated ion peak shape was used rather than a Gaussian to optimise the calibrant ion fits. Mass accuracy was in the range 10-20 ppm for all calibrant ions.

On December 2 and 3, 2014, elevated aerosol chloride was observed at the Neumayer station (Fig. S8-S9). Air mass back trajectories (Global Data Assimilation System (GDAS) air mass backward trajectories using the NOAA Hybrid Single-Particle Lagrangian Integrated Trajectory model (HYSPLIT, v4.9, (Draxler and Rolph, 2013)) show that the air mass was transported along the Antarctic coastline in low altitudes during the previous days, pointing to the influence of sea-salt as an explanation for the observed chloride concentrations of up to  $300 \text{ ng m}^{-3}$  (Fig. S9). Neither MSA, proxied by  $m/Q$  79, nor organic aerosol was elevated during this period. Peak-fitting was conducted on the mass spectra from this episode to i) demonstrate the presence of sea-salt related compounds, and ii) generate a time-series for  $\text{NaCl}^+$ , separated from its isobaric organic interference(s). The Chloride ions  $^{35}\text{Cl}^+$  and  $^{37}\text{Cl}^+$  have only relatively tiny interferences in ToF-ACSM mass spectra and thus no meaningful additional information can be expected to be gained from peak-fitting relative to the integrated peak data, except perhaps in exceptionally-large organic plume cases.

Several ions attributable to sea salt (following Schmale et al, 2013.), such as  $\text{Na}^{35}\text{Cl}^+$  (57.958 Th),  $\text{Na}^{37}\text{Cl}^+$  (59.956 Th),  $\text{Fe}^{35}\text{Cl}_2^+$  (125.87 Th) and  $\text{Fe}^{37}\text{Cl}^{35}\text{Cl}^+$  (127.87 Th) could be identified in the average mass spectrum from this period, as shown in Fig. 13. In the case of  $\text{NaCl}^+$ , three interfering isobaric organic ions are known to be visible in ToF-ACSM mass spectra; at this mass resolving power it is not possible to state which of these are observed here, although the oxygenated peak  $\text{C}_3\text{H}_6\text{O}^+$  is a likely candidate and is demonstrated in Fig. 13. However, irrespective of the interference(s) chosen, sensitivity of the fitted intensity of  $\text{NaCl}^+$  to a 100 ppm mass calibration perturbation was  $\sim 5\%$ , indicating that the majority of the difference signal at 58 Th could indeed be attributed to this ion.

The  $\text{FeCl}^+$  ions are shown as a further example of sea salt compounds that could be unambiguously identified in the Neumayer-data. The centre panel in Fig. 13 shows a portion of the average mass spectrum together with peak-fitting curves for the period during which elevated chloride was observed. The mass calibrant ion  $\text{C}_2\text{Cl}_3\text{H}^+$  at 130 Th is visible in addition to unknown background ion(s) at 126 and 128 Th. For the difference mass spectrum, however, these background ions contribute only to the noise and two aerosol signals are resolvable above the noise level, defined as 3 times the standard deviation over the adjacent mass range. These signals are well represented by the  $\text{Fe}^{35}\text{Cl}_2^+$  and  $\text{Fe}^{37}\text{Cl}^{35}\text{Cl}^+$  isotopes; the mass excess of these aerosol peaks is significantly ( $\sim 1500$  ppm) less than the background peaks observed for the total mass spectrum. We note that it is almost certain that the signal from a multitude of unresolvable organic ions combines together to give the apparent single background peak, but in this analysis we are only concerned with the relatively well-separated sea salt signals. Further support



to their identification is given by the ratio of the signal intensities.  $^{37}\text{Cl}$  exhibits only 32 % the abundance of the  $^{35}\text{Cl}$  isotope, thus an intensity ratio of 67 % is expected between these peaks, in acceptable agreement with the observed 59 % from the fitted peak intensities given the weak signal levels.

5 The time-series of fitted peak intensities also supports the hypothesis that the aerosol chloride can be attributed to sea salt, for the trends of  $\text{Cl}^+$  and  $\text{NaCl}^+$  are moderately correlated ( $R^2 = 0.4$ ), as shown in Fig. 14. The signal intensities of  $\text{NaCl}^+$  are weak and the noise in the organic background signal at 58 Th from  $\text{C}_3\text{H}_6\text{O}^+$  is significant, but it shows no apparent correlation with the chloride signal.

#### 4.5. Methanesulphonic acid

10 Oceans release dimethyl sulphide, which is further oxidized to several sulphur compounds,  $\text{SO}_2$ ,  $\text{H}_2\text{SO}_4$  and MSA (Gondwe et al., 2003; Yin et al., 1990). Previous studies have demonstrated that the AMS can be used to measure MSA concentrations of submicron particles (Phinney et al., 2006; Schmale et al., 2013).

15 From January 7-13<sup>th</sup>, 2015, elevated sulphate (up to 2000  $\text{ng m}^{-3}$ ) and MSA concentrations were observed at the Neumayer station (Fig. S10). At Neumayer, the interference from isobaric ions was very low (Fig. S11). All typical MSA fragments (Schmale et al., 2013, Phinney et al., 2006) were relatively strong signals relative to their isobaric interferences and could be straightforwardly identified in the mass spectra:  $\text{CHS}^+$  (44.98 Th),  $\text{CH}_3\text{S}^+$  (47.00 Th),  $\text{HSO}_2^+$  (64.97 Th),  $\text{CH}_2\text{SO}_2^+$  (77.98 Th),  $\text{CH}_3\text{SO}_2^+$  (78.99 Th) and  $\text{CH}_4\text{SO}_3^+$  (95.99 Th) (Fig. 15, Table 2). A good correlation between the main ions ( $\text{HSO}_2^+$ ,  $\text{CH}_3\text{SO}_2^+$ , and  $\text{CH}_4\text{SO}_3^+$ ) with highest signals was observed (Fig. S12, Table S1). However, we note that for all MSA ions the separation from isobaric ions was low ( $X=0.2-0.4$ , thus increasing the uncertainty of the results. In typical conditions with larger background and/or organic signals, this analysis would become difficult and uncertainties large. In clean conditions ToF-ACSM provided the possibility to discern between and measure both sulphate and MSA fragments, which combined with meteorological data could be used to e.g. to further study the CLAW hypothesis (Charlson et al., 1987).

#### 4.6. Metals

25 Data collected in an underground mine is used to study the peak-fitting of ions from semi-volatile metals. It has been demonstrated that the ToF-AMS, upon whose technology the ACSM is based, is capable of detecting ions associated with the metals Cu, Zn, As, Se, Sn, and Sb (Salcedo et al, 2012). Further semi-volatile elements may also be measurable based on their melting or thermal decomposition points (Drewnick et al., 2015). In the mine environment it is to be expected that metallic elements comprise a significant fraction of the aerosol mass (Csavina et al., 2012). This dataset is thus a good example for a first assessment of the capability of the ToF-ACSM to detect metal species. The ions of these species tend to have large mass excesses and are often separated from their neighbouring ions by  $X > 1$ , indicating that peak-fitting should be able to resolve



their signals. These peak separations are given in Table 3 for the isotopes of the metals reported detectable by Salcedo et al. (2012).

High signal levels, such as those observed in the mine (up to  $200 \mu\text{g m}^{-3}$ ), clearly improve peak-fitting, as the description of the peak shape is well defined by the discrete data points with high signal/noise along the mass spectrum continuum. However, the multiple interferences at nearly every isobar precludes a truly accurate mass calibration and certain assumptions must be made when performing this analysis step. Consequently, a careful sensitivity analysis must be performed before drawing conclusions from the fitted peak intensities. To highlight the performance of the instrument and fitting procedure in measuring changes in mass component intensities, a period at the end of a working day was chosen for detailed analysis, where the organic mass loading in the mine falls sharply from  $> 30$  to  $< 3 \mu\text{g m}^{-3}$  over a 2 hour period.

As many of the metals isotopes exhibit mass excesses that differ significantly from other (in most cases organic) peaks in the MS, representation of the fitted position in  $m/Q$  of each isobaric peak in a mass excess plot can be used to highlight features of interest, as shown in Fig. 16. Certain peaks stand out from the general pattern as having mass excesses that deviate from the general trend, principally those from  $\text{SO}_x$  (48, 64, 66) and  $\text{As}_x$  (75, 150). It is noted that there is a contribution from  $^{66}\text{Zn}^+$  at 66 Th which also contributes to the observed negative mass excess. A more detailed investigation was thus undertaken to assess potential signals from the As and Zn ions.

#### 4.6.1. Mass calibration

The high mass loadings encountered during the mine study led to a large instrument background, which remained elevated overnight. The tungsten isotope pattern was occluded and these ions could not be used in the mass calibration. However, the pattern of the trichloroethylene isotopes was evident during cleaner periods, albeit not without interference from overlapping organic background peaks. An example MS is shown in Fig. S13; the peaks at the isobars 130 and 132 Th, where the principal ions of trichloroethylene show, are approximately 3 times as large as many of the surrounding organic background peaks. As no other identified isolated ions were available at masses greater than 44 Th ( $\text{CO}_2^+$ ), an attempt was made to constrain the high-end of the mass calibration by employing the mass-compensation technique described in section 3.2.2.2. As a result, the exact mass of the trichloroethylene ions in the mass calibration was increased by 0.04 Th or  $\sim 300$  ppm (the corresponding mass excess plot is given in Fig. S14. These ions, together with  $\text{N}_2^+$ ,  $\text{O}_2^+$  and  $\text{CO}_2^+$ , were used to apply a mass calibration for the entire time period of study. The compensation technique could not have been utilised for mass spectra during the working hours of the mine as the organic mass loading was too high (and the Trichloroethylene peaks thus obscured to the extent that the calibration compensation technique would introduce unacceptably large errors into the fitted parameters). It is noted that, relative to the mass axis derived using this calibration technique, calibrating on the air peaks alone would have led to a mass offset of -57 ppm at 150 Th (ie, extrapolating to the high end of the MS). A sensitivity analysis must therefore account for mass calibration perturbations at least as large as this, preferably greater.



#### 4.6.2. Time series of metal ions

After application of the mass calibration and determination of the peak width and shape using the methods described in 3.1, peak-fitting was performed on the mine data with a peak list specifically chosen to assess the potential of the ToF-ACSM to deconvolve the metal ion signals from the interfering organic peaks. An example of the aerosol signal derived from the fitted peak intensities is shown in Fig. 17 for the Arsenic ion  $As_2^+$  (An example mass spectrum from this time series showing the peak fits is shown in Fig. S15). Three ions have been fitted to the isobaric peak,  $As_2^+$ ,  $C_4H_6O_6^+$  and  $C_{10}H_{14}O^+$ . The two organic ions are closely spaced ( $X < 0.4$ ) and we emphasise that we do not attempt to conclude whether the organic signal at 150 Th is attributable to either  $C_4H_6O_6^+$  or  $C_{10}H_{14}O^+$  (or otherwise) but seek only to separate the metal and organic signals as a whole. Although it was demonstrated for nitrate that highly-overlapping peaks with similar  $X$  values could be deconvolved, the uncertainty in the mass calibration is much larger in this example, precluding the reliable separation of the organic signals. However,  $As_2^+$  and its assumed closest neighbour  $C_4H_6O_6^+$  are separated by  $X \sim 1.0$  and thus should be resolvable according to the results of Cubison and Jimenez (2015). As Figure 17 shows, this does indeed appear to be the case. Both the organic and metal signals decrease in intensity at the end of the working day, but the organic remains at a measurable non-zero value overnight whereas the  $As_2^+$  decreases below the detection limit. A similar trend was apparent for the  $As^+$  ion (scatter plot in Fig. S16). It is noted that no attempt is made here to derive the true mass loadings of the metal and organic components, whose calculation is outside the scope of this peak-fitting paper and would require application of relative ionization efficiencies which are still poorly understood (Salcedo et al., 2012). Finally, it is observed that use of the “Fast-MS” sampling technique described by Kimmel et al. (2011) allows time-resolved detection of slowly evaporating components in the difference data (ambient minus filter).

#### 4.6.3. Sensitivity analysis

Given the assumptions made in applying the mass calibration, assessment of the sensitivity of the fitted peak intensities to calibration perturbations, analogously as was described in section 4.2 for nitrate, was particularly important for this dataset. Figure 18 shows the results of this sensitivity analysis at 150 Th, with fitted ions  $As_2^+$ ,  $C_4H_6O_6^+$  and  $C_{10}H_{14}O^+$  and an especially large mass calibration perturbation of  $\pm 200$  ppm, to reflect the low confidence in the mass calibration. From these analyses we conclude that i) the integrated area can be reconstructed from summed fitted peak intensities to within a few percent (excluding points with weak signals less than 2 ions/s where counting error is large), ii) the fitted intensity of  $As_2^+$  is not sensitive to calibration imperfections, exhibiting  $\Delta_I \sim 20\%$  with a 200 ppm offset, and iii) the predicted imprecision on this intensity,  $\sigma_I$ , is also (coincidentally)  $\sim 20\%$ . Although this example presents a truly challenging peak-fitting scenario with limited signal, a large degree of peak overlap and an uncertain mass calibration, it can be confidently concluded that there is a non-negligible contribution to mass loading from the metal ion  $As_2^+$ . One may also draw conclusions based on the actual fitted peak intensities provided they hold true for changes of  $\pm 20\%$ .



Further analyses were conducted for other potential metal ions in the mine dataset, showing good evidence for the presence of the Zn isotopes (Fig. S17). A weak but non-zero signal was also found for In<sup>+</sup> (Fig. S18). Other potential candidates showed either negligible signal or sensitivity analyses showed their fitted intensities to be unreliable (e.g. for Cu<sup>+</sup>, Fig. S19).

#### 4.7 Refinement of HOA/OOA constants

5 Ng et al. (2011a) proposed a simple methodology, colloquially known in the AMS community as “poor woman’s PMF”, for estimating the concentrations of oxygenated organic aerosol (OOA) and hydrocarbon-like organic aerosol (HOA) from the integrated signals at 44 and 57 Th, giving the relationship for HOA  $\sim 13.4 * (C_{57} - a * C_{44})$ , where  $C_x$  represents the integrated signal over the isobar peak at  $m/Q = X$ . The constant  $a$  was estimated as 0.1 and accounts for the predicted concentration of the interfering oxygenated ion C<sub>3</sub>H<sub>5</sub>O<sup>+</sup> at 57 Th where the majority of ion signal can be attributed to C<sub>4</sub>H<sub>7</sub><sup>+</sup>. These two ions  
10 are separated by  $X = 0.6$  Th at  $m/dm = 450$  and are thus, with some degree of uncertainty, separable in ToF-ACSM mass spectra. Thus a linear regression can be made of the fitted ion intensities of CO<sub>2</sub><sup>+</sup> and C<sub>3</sub>H<sub>5</sub>O<sup>+</sup> to calculate the constant  $a$  for the dataset under analysis, as shown for the SMEARIII dataset in Figure S20. The derived slope for the SMEARIII data of 0.04 led to an increase in estimated HOA concentrations of 6% with respect to using the default value of 0.1.

#### 4.8. Oxidation state from analysis of mass excess

15 The limited mass resolving power of the ETOF-equipped ToF-ACSM precludes the calculation of the oxidation state (see Kroll et al., 2011) and O/C and H/C ratios using the elemental analysis approach commonly employed in HR-ToF-AMS analysis and detailed in Aiken et al. (2007). However, it was recently shown using chemical ionisation data how the carbon oxidation state approximately follows the observed mass excess of the fitted ion peaks (Stark et al., 2015). Given that this principle of mass excess variation applies generally to all organic molecules irrespective of the ionisation technique, a similar  
20 mass excess analysis was thus applied to the SMEARIII data to investigate the aerosol oxidation state. Stark et al. used the higher mass resolving power of their data together with comprehensive ion lists to analyse the mass excess of all the fitted ions using the constrained peak-fitting methods described in section 3. A mass resolving power of  $\sim 500$  precludes this approach, so instead, the simpler bulk mass spectrum method also proposed by Stark et al. was employed. A mean average of the mass excess for the mass spectral data points for each isobaric MS peak between 41 and 100 Th, except those known to be influenced  
25 by inorganic ions such as SO<sup>+</sup>, was generated by weighting to the observed signal level at each point. The range and weighted mean average of the mass excess values are plotted for a time-series of a few days in Fig. 19. The OOA and HOA components were also calculated following the so-called “poor woman’s PMF” methodology of Ng et al. (2011a) and the relative fraction of OOA is also shown. The average mass excess exhibits a clear anti-correlation with the OOA fraction with  $R^2 = 0.88$ , supporting the validity of the method for the assessment of aerosol oxidation.



The parameterisation proposed by Stark et al. (2015, see also suppl. info) is used to estimate the bulk aerosol carbon oxidation state,  $OS_C$ , from the mass excess values. The values lie between -1.6 and -0.8 and are consistent with HOA and “fresh” semi-volatile OOA (SV-OOA) (Kroll et al., 2011), as expected for an urban measurement location.

To support the validity of this method, the estimated oxidation state value was also analogously calculated from spectra generated for a range of organic standards using the data presented in Canagaratna et al. (2015). For each compound, synthetic ETOF spectra were created by convolving a typical ETOF transfer function with the list of fitted ions and their intensities from the HR-ToF-AMS peak-fitting results of Canagaratna et al. (2015). The estimated oxidation state calculated from these spectra is compared to the real values in Fig. 20, exhibiting  $R^2 = 0.77$  and quantitative agreement to within 1.5 %. This indicates that ETOF mass spectra have sufficient mass resolving power for the successful quantitative application of this method.

The parameterisations of Aiken et al. (2008) and Canagaratna et al. (2015) are often utilised to estimate the aerosol O:C ratio from integrated nominal-mass data based on the ratio of the integrated organic signal at 44 Th to that of all organic peaks, known as  $f_{44}$ . However, discrepancies were noted in  $f_{44}$  between instruments during the recent ACTRIS ACSM intercomparison exercise (Crenn et al., 2015; Fröhlich et al., 2015). As the mass excess parameterisation for oxidation state estimation described here depends on many more signals than just  $CO_2^+$ , it could potentially be a more reproducible method for investigating aerosol oxidation; this reproducibility across instruments should be a focus of future intercomparison exercises. Variability in mass calibration is a potential source of bias; however, an extrapolated calibration using just the air peaks would be sufficient to capture the mass range considered here (under 100 Th) and could be systematically applied. We note also that application of a 50 ppm mass calibration bias introduces a corresponding bias in  $OS_C$  of only  $\sim 0.2$ .

## 5. Conclusions

The separation of isobaric ions using constrained peak-fitting in data from the recently developed time-of-flight aerosol chemical speciation monitor (ToF-ACSM) was investigated. Details of the constrained peak-fitting methodology were given and a thorough discussion on mass calibration techniques presented. From the peak-fitting results, it was demonstrated for the atmospherically-relevant example datasets used that:

- The intensities of the ammonium ions  $NH_x^+$  could not be reliably deconvolved from those of their relatively large isobaric interferences.
- The intensities of the nitrate ions  $NO^+$  and  $NO_2^+$  could be reliably deconvolved from their heavily-overlapping isobaric organic interferences owing to high confidence in the mass calibration in the appropriate regions of the mass spectrum ( $\Delta_I < 10\%$ ,  $\sigma_I < 10\%$ ).
- The intensities of the sulphate ions  $SO^+$  and  $SO_2^+$ , and to a lesser extent  $SO_3^+$ ,  $HSO_3^+$  and  $H_2SO_4^+$ , could also be reliably deconvolved from their isobaric organic interferences ( $\Delta_I < 10\%$ ,  $\sigma_I < 10\%$  for  $Org/SO_4 \ll 5$ ).
- Sodium chloride and other sea-salt related compounds could be positively identified in the mass spectrum.



- Compounds originating from MSA could be positively identified in the mass spectrum from a clean location.
- Time-series signals from some metal compounds that could be vapourised at 600 °C could be successfully deconvolved from their organic isobaric interferences ( $\Delta I < 25\%$ ,  $\sigma_I < 20\%$  for organic/metal intensity ratio  $\sim 2$ ).
- The constants used to implement the “poor-woman’s PMF” approach for the estimation of HOA and OOA mass loadings can be improved by a few percent using peak-fitting results.
- Oxidation state can be estimated directly from ToF-ACSM mass spectra using the formula of Stark et al. (2015); this parameterisation exhibited a good correlation ( $R^2 = 0.77$ ) to results from HR-ToF-AMS elemental analyses of organic standards. Intercomparisons between multiple co-located instruments are required in the future to further validate this approach.

5

10 It is noted that the actual values of  $\Delta I$  and  $\sigma I$  obtained for a given dataset will depend on the relative signal strengths of the fitted ions. Thus the values quoted here are pertinent only for the (atmospherically relevant, but specific) examples we have presented and the reader is encouraged to evaluate these parameters on a case-by-case basis.

Owing to the limited mass resolving power of the ToF-ACSM instrument, the particular ions used during constrained peak-fitting ought to be carefully considered based on targeted analyses, rather than taking the blanket approach of fitting everything as is generally conducted for HR-ToF-AMS data. As a guide, we summarise the ions considered in this study in table 4, together with a recommendation for mass calibration perturbations to be used in sensitivity analyses. Additionally, we report the approximate maximum peak intensity ratios, for the case where the ion signal of interest is weaker than its influences, that would be required for a relative fitted intensity precision of 25%.

15

This list is not exhaustive; for example, Fröhlich et al. (2013) already showed successful separation of the isobaric organic signals  $C_2H_3O^+$  and  $C_3H_7^+$  at 43 Th. The intensities of other peaks, particularly those compounds with more negative mass excesses than typical atmospheric organics, should also be determinable using constrained peak-fitting.

20

Finally, we note that the techniques presented here are applicable to any data analysed using the constrained fitting approach and not just the ToF-ACSM. In any case, consideration of parameters such as the normalised peak separation  $X$ , bias in fitted intensity owing to mass calibration perturbations  $\Delta I$  and estimated relative intensity imprecision  $\sigma_I$  is to be recommended when discussing peak-fitting results.

25

## Acknowledgements

Funding from the Finnish Funding Agency for Technology and Innovation (TEKES) in the Green Mining program (HIME-project) and Academy of Finland (ACPANT) is gratefully acknowledged. The Kemi Mine staff are gratefully acknowledged for their help during the measurement campaign. John Shilling is recognised for his unpublished work on the use of fitting constraints in AMS mass calibration. We thank Patrick Sturm for the EI-TOF data. The Neumayer III staff are gratefully

30



acknowledged for their help in running the instruments. Marc Gonin, Jose Jimenez, John Jayne, Phil Croteau and Leah Williams are acknowledged for useful discussions on this topic. We thank the many Tofware users whose feedback during development has been invaluable.

## 5 References

- Aiken, A.C., DeCarlo, P. F., and Jimenez, J. L.: Elemental Analysis of Organic Species with Electron Ionization High-Resolution Mass Spectrometry, *Anal. Chem.*, 79, 8350–8358, doi:10.1021/ac071150w, 2007.
- Aiken, A. C., DeCarlo, P. F., Kroll, J. H., Worsnop, D. R., Huff-man, J. A., Docherty, K., Ulbrich, I. M., Mohr, C., Kimmel, J.R., Sueper, D., Sun, Y., Zhang, Q., Trimborn, A., Northway, M., Ziemann, P. J., Canagaratna, M. R., Onasch, T. B., Alfarra, M.R., Prevot, A. S. H., Dommen, J., Duplissy, J., Metzger, A., Baltensperger, U., and Jiménez, J. L.: O/C and OM/OC Ratios of Primary, Secondary, and Ambient Organic Aerosols with a HighResolution Time-of-Flight Aerosol Mass Spectrometer, *Environ. Sci. Technol.*, 42, 4478–4485, 2008.
- Allan, J. D., Coe, H., Bower, K. N., Alfarra, M. R., Delia, A. E., Jimenez, J. L., Middlebrook, A. M., Drewnick, F., Onasch, T. B., Canagaratna, M. R., Jayne, J. T., and Worsnop, D.R.: Technical Note: Extraction of Chemically Resolved Mass Spectra from Aerodyne Aerosol Mass Spectrometer Data, *Journal of Aerosol Science*, 35, 909-922, 2004.
- Canagaratna, M. R., Jimenez, J. L., Kroll, J. H., Chen, Q., Kessler, S. H., Massoli, P., Hildebrandt Ruiz, L., Fortner, E., Williams, L. R., Wilson, K. R., Surratt, J. D., Donahue, N. M., Jayne, J. T., and Worsnop, D. R.: Elemental ratio measurements of organic compounds using aerosol mass spectrometry: characterization, improved calibration, and implications, *Atmos. Chem. Phys.*, 15, 253-272, doi:10.5194/acp-15-253-2015, 2015.
- Charlson, R. J., Lovelock, J. E., Andreae, M. O., and Warren, S. G.: Oceanic phytoplankton, atmospheric sulphur, cloud albedo and climate, *Nature*, 326, 655-661, 1987.
- Corbin, J., Othman, A., D. Allan, J., R. Worsnop, D., D. Haskins, J., Sierau, B., Lohmann, U., and A. Mensah, A.: Peak-fitting and integration imprecision in the Aerodyne aerosol mass spectrometer: effects of mass accuracy on location-constrained fits, *Atmos. Meas. Tech.*, 8, 4615-4636, doi:10.5194/amt-8-4615-2015, 2015.
- Crenn, V., Sciare, J., Croteau, P. L., Verlhac, S., Fröhlich, R., Belis, C. A., Aas, W., Äijälä, M., Alastuey, A., Artiñano, B., Baisnée, D., Bonnaire, N., Bressi, M., Canagaratna, M., Canonaco, F., Carbone, C., Cavalli, F., Coz, E., Cubison, M. J., Esser-Gietl, J. K., Green, D. C., Gros, V., Heikkinen, L., Herrmann, H., Lunder, C., Minguillón, M. C., Močnik, G., O'Dowd, C. D., Ovadnevaite, J., Petit, J.-E., Petralia, E., Poulain, L., Priestman, M., Riffault, V., Ripoll, A., Sarda-Estève, R., Slowik, J. G., Setyan, A., Wiedensohler, A., Baltensperger, U., Prévôt, A. S. H., Jayne, J. T., and Favez, O.: ACTRIS ACSM intercomparison – Part I: Reproducibility of concentration and fragment results from 13 individual Quadrupole Aerosol Chemical Speciation Monitors (Q-ACSM) and consistency with Time-of-Flight ACSM (ToF-ACSM), High



- Resolution ToF Aerosol Mass Spectrometer (HR-ToF-AMS) and other co-located instruments, *Atmos. Meas. Tech. Discuss.*, 8, 7239-7302, doi:10.5194/amt-d-8-7239-2015, 2015.
- Csavina, J., Field, J., Taylor, M. P., Gao, S., Landázuri, A., Betterton, E. A., and Sáez, A. E.: A review on the importance of metals and metalloids in atmospheric dust and aerosol from mining operations. *Sci. Total Environ.*, 433, 58-73, 2012.
- 5 Cubison, M. J. and Jimenez, J. L.: Statistical precision of the intensities retrieved from constrained fitting of overlapping peaks in high-resolution mass spectra, *Atmos. Meas. Tech.*, 8, 2333-2345, doi:10.5194/amt-8-2333-2015, 2015.
- DeCarlo, P. F., Kimmel, J. R. Trimborn, A. Northway, M. J. Jayne, J. T. Aiken, A. C., Gonin, M., Fuhrer, K., Horvath, T., Docherty, K., Worsnop, D. R. and Jimenez, J. L.: Field-Deployable, High-Resolution, Time-of-Flight Aerosol Mass Spectrometer, *Analytical Chemistry*, 78, 8281-8289, 2006.
- 10 Draxler, R. R., Rolph, G. D.: HYSPLIT (HYbrid Single-Particle Lagrangian Integrated Trajectory) Model. NOAA air Resources Laboratory, Silver Spring, MD. Access via NOAA ARL READY Website. <http://ready.arl.noaa.gov/HYSPLIT.php>, 2013.
- Drewnick, F., Hings, S. S., DeCarlo, P., Jayne, J. T., Gonin, M., Fuhrer, K., Weimer, S., Jimenez, J. L., Demerjian, K. L., Borrmann, S., and Worsnop, D. R.: A New Time-of-Flight Aerosol Mass Spectrometer (TOF-AMS)—Instrument  
15 Description and First Field Deployment, *Aer. Sci. Tech.*, 39, 637-658, 2005.
- Fröhlich, R., Cubison, M. J., Slowik, J. G., Bukowiecki, N., Prévôt, A. S. H., Baltensperger, U., Schneider, J., Kimmel, J. R., Gonin, M., Rohner, U., Worsnop, D. R., and Jayne, J. T.: The ToF-ACSM: a portable aerosol chemical speciation monitor with TOFMS detection, *Atmos. Meas. Tech.*, 6, 3225-3241, doi:10.5194/amt-6-3225-2013, 2013.
- Fröhlich, R., Crenn, V., Setyan, A., Belis, C. A., Canonaco, F., Favez, O., Riffault, V., Slowik, J. G., Aas, W., Aijälä, M.,  
20 Alastuey, A., Artiñano, B., Bonnaire, N., Bozzetti, C., Bressi, M., Carbone, C., Coz, E., Croteau, P. L., Cubison, M. J., Esser-Gietl, J. K., Green, D. C., Gros, V., Heikkinen, L., Herrmann, H., Jayne, J. T., Lunder, C. R., Minguillón, M. C., Močnik, G., O'Dowd, C. D., Ovadnevaite, J., Petralia, E., Poulain, L., Priestman, M., Ripoll, A., Sarda-Estève, R., Wiedensohler, A., Baltensperger, U., Sciare, J., and Prévôt, A. S. H.: ACTRIS ACSM intercomparison – Part 2: Intercomparison of ME-2 organic source apportionment results from 15 individual, co-located aerosol mass spectrometers,  
25 *Atmos. Meas. Tech. Discuss.*, 8, 1559-1613, doi:10.5194/amt-d-8-1559-2015, 2015.
- Canagaratna, M. R., Jimenez, J. L., Kroll, J. H., Chen, Q., Kessler, S. H., Massoli, P., Hildebrandt Ruiz, L., Fortner, E., Williams, L. R., Wilson, K. R., Surratt, J. D., Donahue, N. M., Jayne, J. T., and Worsnop, D. R.: Elemental ratio measurements of organic compounds using aerosol mass spectrometry: characterization, improved calibration, and implications, *Atmospheric Chemistry and Physics*, 15, 253-272, 2015.



- Gondwe, M., Krol, M., Gieskes, W., Klaassen, W. and de Baar, H.: The contribution of ocean-leaving DMS to the global atmospheric burdens of DMS, MSA, SO<sub>2</sub>, and NSS SO<sub>4</sub>, *Global Biogeochem. Cycles*, 17, 1056, doi:10.1029/2002GB001937, 2003.
- IPCC, 2013: *Climate Change 2013: The Physical Science Basis. Contribution of Working Group I to the Fifth Assessment Report of the Intergovernmental Panel on Climate Change* [Stocker, T.F., D. Qin, G.-K. Plattner, M. Tignor, S.K. Allen, J. Boschung, A. Nauels, Y. Xia, V. Bex and P.M. Midgley (eds.)]. Cambridge University Press, Cambridge, United Kingdom and New York, NY, USA, 1535 pp.
- 5 Jayne, J. T., Leard, D. C., Zhang, X., Davidovits, P., Smith, K. A., Kolb, C. E., Worsnop, D. R.: Development of aerosol mass Spectrometer for Size and Composition Analysis of Submicron Particle, *aerosol Science and Technology*, 33, 49-70, 2000.
- 10 Jimenez, J.L., Jayne, J.T. Shi, Q. Kolb, C.E. Worsnop, D.R. Yourshaw, I. Seinfeld, J.H. Flagan, R.C., Zhang, X., Smith, K. A., Morris, J. and Davidovits, P.: Ambient Aerosol Sampling with an Aerosol Mass Spectrometer, *J. Geophys. Res.-Atmospheres*, 108(D7), 8425, doi:10.1029/2001JD001213, 2003.
- Junninen, H., Ehn, M., Petäjä, T., Luosujärvi, L., Kotiaho, T., Kostianen, R., Rohner, U., Gonin, M., Fuhrer, K., Kulmala, M., and Worsnop, D. R.: A high-resolution mass spectrometer to measure atmospheric ion composition, *Atmos. Meas. Tech.*, 3, 1039-1053, doi:10.5194/amt-3-1039-2010, 2010.
- 15 Järvi, L., Hannuniemi, H., Hussein, T., Junninen, H., Aalto, P. P., Hillamo, R., Mäkela, T., Keronen, P., Siivola, E., Vesala, T., and Kulmala, M.: The urban measurement station SMEAR III: Continuous monitoring of air pollution and surface-atmosphere interactions in Helsinki, Finland, *Boreal Environ Res*, 14, 86-109, 2009.
- Kimmel, J. R., Farmer, D. K., Cubison, M. J., Sueper, D., Tanner, C., Nemitz, E., Worsnop, D.R., Gonin, M. and Jimenez J. L.: Real-time Aerosol Mass Spectrometry with Millisecond Resolution. *International Journal of Mass Spectrometry*, 303(1), 15-26, 2011. DOI:10.1016/j.ijms.2010.12.004.
- 20 Kroll, J. H., Donahue, N. M., Jimenez, J. L., Kessler, S. H., Canagaratna, M. R., Wilson, K. R., Altieri, K. E., Mazzoleni, L. R., Wozniak, A. S., Bluhm, H., Mysak, E. R., Smith, J. D., Kolb, C.E., and Worsnop D.R.: Carbon Oxidation State as a Metric for Describing the Chemistry of Atmospheric Organic Aerosol, *Nature Chemistry*, 3, 133-139, DOI:10.1038/NCHEM.948, 2011.
- 25 Korhonen, H., Carslaw, K. S., Spracklen, D. V., Mann, G. W., and Woodhouse, M. T.: Influence of oceanic dimethyl sulfide emissions on cloud condensation nuclei concentrations and seasonality over the remote Southern Hemisphere oceans: A global model study, *Journal of Geophysical Research*, 113, 10.1029/2007jd009718, 2008.
- Lawson, C. L. and Hanson, R. J.: *Solving Least Squares Problems*, SIAM, 1995.



Meija, J. and Caruso, J. A.: Deconvolution of isobaric interferences in mass spectra, *J Am Soc Mass Spectrom.*, 15(5),654-658, 2004.

Müller, M., Mikoviny, T., Jud, W., D'Anna, B. and Wisthaler, A.: A new software tool for the analysis of high resolution PTR-TOF mass spectra, *Chemometrics and Intelligent Laboratory Systems*, 127, 158–165, 2013.

5

Ng, N. L., Canagaratna, M. R., Jimenez, J. L., Zhang, Q., Ulbrich, I. M., and Worsnop, D. R.: Real-time methods for estimating organic component mass concentrations from aerosol mass spectrometer data, *Environ Sci Technol*, 45, 910-916, 2011a.

10

Ng, N. L., Herndon, S. C., Trimborn, A., Canagaratna, M. R., Croteau, P. L., Onasch, T. B., Sueper, D., Worsnop, D. R., Zhang, Q., Sun, Y. L., and Jayne, J. T.: An Aerosol Chemical Speciation Monitor (ACSM) for Routine Monitoring of the Composition and Mass Concentrations of Ambient Aerosol. *Aer. Sci. Tech.*, 45(7), 780-794, DOI: 10.1080/02786826.2011.560211, 2011b.

15

Ortega, A. M., Day, D. A., Cubison, M. J., Brune, W. H., Bon, D., de Gouw, J. A., and Jimenez, J. L.: Secondary organic aerosol formation and primary organic aerosol oxidation from biomass burning smoke in a flow reactor during FLAME-3, *Atmos. Chem. Phys.*, 13, 13799-13851, 2013

Phinney, L., Leaitch, W., Lohmann, U., Boudries, H., Worsnop, D. R., Jayne, J. T., Toom-Saunty, D., Wadleigh, M., Sharma, S., and Shantz, N.: Characterization of the aerosol over the sub-arctic north east Pacific Ocean, *Deep Sea Research Part II: Topical Studies in Oceanography*, 53, 2410-2433, 10.1016/j.dsr2.2006.05.044, 2006.

20

Pope, C. A., Dockery, D. W.: Health Effects of Fine Particulate Air Pollution: Lines that Connect, *J. Air & Waste Manage. Assoc.*, 56, 709-742, 2006.

Salcedo, D., Laskin, A., Shutthanandan, V. and Jimenez, J.L.: Feasibility of the Detection of Trace Elements in Particulate Matter Using Online High-Resolution Aerosol Mass Spectrometry, *Aer. Sci. Tech.*, 46, 1187-1200, DOI: 10.1080/02786826.2012.701354, 2012.

25

Schmale, J., Schneider, J., Nemitz, E., Tang, Y. S., Dragosits, U., Blackall, T. D., Trathan, P. N., Phillips, G. J., Sutton, M., and Braban, C. F.: Sub-Antarctic marine aerosol: dominant contributions from biogenic sources, *Atmos. Chem. Phys.*, 13, 8669-8694, 10.5194/acp-13-8669-2013, 2013.

Stark, H., Yatavelli, R. N. L., Thompson, S. L., Kimmel, J. R., Cubison, M. J., Chhabra, P. J., Canagaratna, M. R., Jayne, J. T., Worsnop, D. R., Jimenez, J. L.: Methods to extract molecular and bulk chemical information from series of complex mass spectra with limited mass resolution, in review at *Int. J. Mass Spec.*, 2015.



Sueper, D. ToF-AMS High Resolution Analysis Software – Pika, Available at:<http://cires.colorado.edu/jimenez-group/ToFAMSResources/ToFSoftware/> PikaInfo, 2008.

Weller, R., Minikin, A., Wagenbach, D., and Dreiling V.: Characterization of the inter-annual, seasonal, and diurnal variations of condensation particle concentrations at Neumayer, Antarctica, Atmos. Chem. Phys., 11, 13243-13257, 2011.

5 Weller, R., Schmidt, K., Teinilä, K., and Hillamo, R.: Natural new particle formation at the coastal Antarctic site Neumayer, Atmos. Chem. Phys., 15, 11399–11410, 2015.

Yin, F., Grosjean, D., Flagan, R.C. and Seinfeld, J. H.: Photooxidation of dimethyl sulfide and dimethyl disulfide: Mechanisms evaluation, J. Atmos. Chem, 11, 365-399, 1990.

10

#### Tables:

**Table 1:** Mass accuracy in ppm obtained using the true and compensated exact masses for the tungsten ions during mass calibration.

Ion	SF <sub>3</sub> <sup>+</sup>	SF <sub>4</sub> <sup>+</sup>	SF <sub>5</sub> <sup>+</sup>
Using true W+ m/Q	-71	-21	-76
Compensated	-57	-3	-53

15

**Table 2:** Observed MSA ions, their principal isobaric ions and peak separation X

Ion	m/Q (Th)	Principal isobaric ions	Peak separation X
CHS <sup>+</sup>	44.979347	C <sub>2</sub> H <sub>5</sub> O <sup>+</sup> , <sup>13</sup> CO <sub>2</sub>	0.2
CH <sub>3</sub> S <sup>+</sup>	46.994999	CH <sub>3</sub> O <sub>2</sub> <sup>+</sup> , CCl <sup>+</sup>	0.3
HSO <sub>2</sub> <sup>+</sup>	64.969177	C <sub>4</sub> HO <sup>+</sup> , C <sub>5</sub> H <sub>5</sub> <sup>+</sup>	0.4
CH <sub>2</sub> SO <sub>2</sub> <sup>+</sup>	77.977005	C <sub>5</sub> H <sub>2</sub> O <sup>+</sup> , C <sub>6</sub> H <sub>6</sub> <sup>+</sup>	0.3
CH <sub>3</sub> SO <sub>2</sub> <sup>+</sup>	78.984825	C <sub>5</sub> H <sub>3</sub> O <sup>+</sup> , C <sub>6</sub> H <sub>7</sub> <sup>+</sup>	0.3
CH <sub>4</sub> SO <sub>3</sub> <sup>+</sup>	95.987564	SO <sub>4</sub> <sup>+</sup>	0.2



5

**Table 3:** Peak separation  $X$ , normalised to HWHM, of various metals ions from neighbouring ions for instrumental mass resolving power of  $m/dm = 450$ .

Element	Ion	Peak separation $X$ from closest neighbouring ion (normalised to HWHM)
As	$^{75}\text{As}^+$ , $^{75}\text{As}_2^+$	1.0
Cu	$^{63}\text{Cu}^+$	1.0
	$^{65}\text{Cu}^+$	1.2
Sb	$^{121}\text{Sb}^+$	1.2
	$^{123}\text{Sb}^+$	1.0
Se	$^{74}\text{Se}^+$	1.2
	$^{76}\text{Se}^+$ , $^{77}\text{Se}^+$	0.9
	$^{78}\text{Se}^+$	1.1
	$^{80}\text{Se}^+$	0.1
Sn	$^{116}\text{Sn}^+$ , $^{118}\text{Sn}^+$	1.1
	$^{120}\text{Sn}^+$	1.5
Zn	$^{64}\text{Zn}^+$	0.4
	$^{66}\text{Zn}^+$ , $^{67}\text{Zn}^+$ , $^{68}\text{Zn}^+$	1.2
	$^{70}\text{Zn}^+$	1.5

10

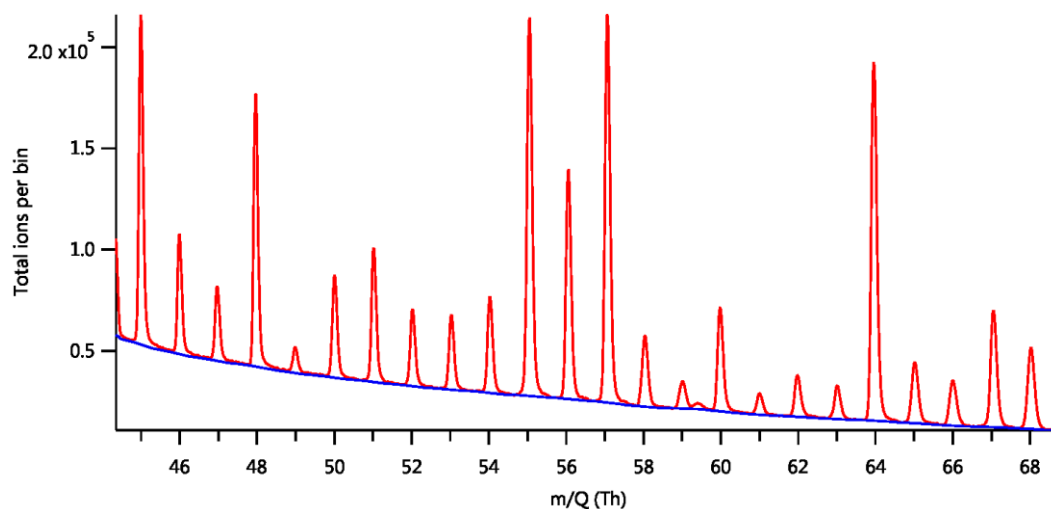


**Table 4:** Summary of ions of interest, their isobaric interferences and recommended magnitudes for calibration sensitivity analyses for various aerosol species measurable with the ToF-ACSM.

Species	Nominal mass (Th)	Ion of interest	Principal interference(s)	Closest peak separation $X$	Sensitivity (ppm)	maximum intensity ratio of influencing peak / peak of interest* to achieve 25 % precision
Nitrate	30	$\text{NO}^+$	$\text{CH}_2\text{O}^+$ , $\text{C}_2\text{H}_6^+$	0.3	10-20	3
Nitrate	46	$\text{NO}_2^+$	$\text{CH}_2\text{O}_2^+$ , $\text{C}_2\text{H}_6\text{O}^+$	0.3	15-20	3
Sulphate	48	$\text{SO}^+$	$\text{C}_4^+$ , $\text{CH}_4\text{O}_2^+$	0.5	20	5
Sulphate	64	$\text{SO}_2^+$	$\text{C}_5\text{H}_4^+$	0.8	50	6
Sulphate	80	$\text{SO}_3^+$	$\text{C}_5\text{H}_4\text{O}^+$ , $\text{C}_6\text{H}_8^+$	0.7	50-100	6
Sulphate	81	$\text{HSO}_3^+$	$\text{C}_5\text{H}_5\text{O}^+$ , $\text{C}_6\text{H}_9^+$	0.7	50-100	6
Sulphate	98	$\text{H}_2\text{SO}_4^+$	$\text{C}_5\text{H}_6\text{O}_2^+$ , $\text{C}_6\text{H}_{10}\text{O}^+$ , $\text{C}_7\text{H}_{14}^+$	0.6	50-100	5
Sodium Chl.	58	$\text{Na}^{35}\text{Cl}^+$	$\text{C}_2\text{H}_2\text{O}_2^+$ , $\text{C}_3\text{H}_6\text{O}^+$ , $\text{C}_4\text{H}_{10}^+$	0.6	50	5
Sodium Chl.	60	$\text{Na}^{37}\text{Cl}^+$	$\text{C}_5^+$ , $\text{C}_2\text{H}_4\text{O}_2^+$ , $\text{C}_3\text{H}_8\text{O}^+$	0.6	50	5
Sodium Chl.	126	$\text{Fe}^{35}\text{Cl}_2^+$	$\text{C}_5\text{H}_2\text{O}_4^+$ , $\text{C}_6\text{H}_6\text{O}_3^+$ , $\text{C}_{10}\text{H}_6^+$	0.8	100	6
Sodium Chl.	128	$\text{Fe}^{37}\text{Cl}^{35}\text{Cl}^+$	$\text{C}_4\text{O}_5^+$ , $\text{C}_6\text{H}_8\text{O}_3^+$ , $\text{C}_{10}\text{H}_8^+$	0.8	100	6
MSA	65	$\text{HSO}_2^+$	$\text{C}_4\text{HO}^+$ , $\text{C}_5\text{H}_5^+$	0.3	50	4
MSA	78	$\text{CH}_2\text{SO}_2$	$\text{C}_5\text{H}_2\text{O}^+$ , $\text{C}_6\text{H}_6^+$	0.3	50-100	4
MSA	79	$\text{CH}_3\text{SO}_2$	$\text{C}_5\text{H}_3\text{O}^+$ , $\text{C}_6\text{H}_7^+$	0.3	50-100	4



Figures:



5

Figure 1: Example of a mass spectral baseline determined using the methodology described in the text.

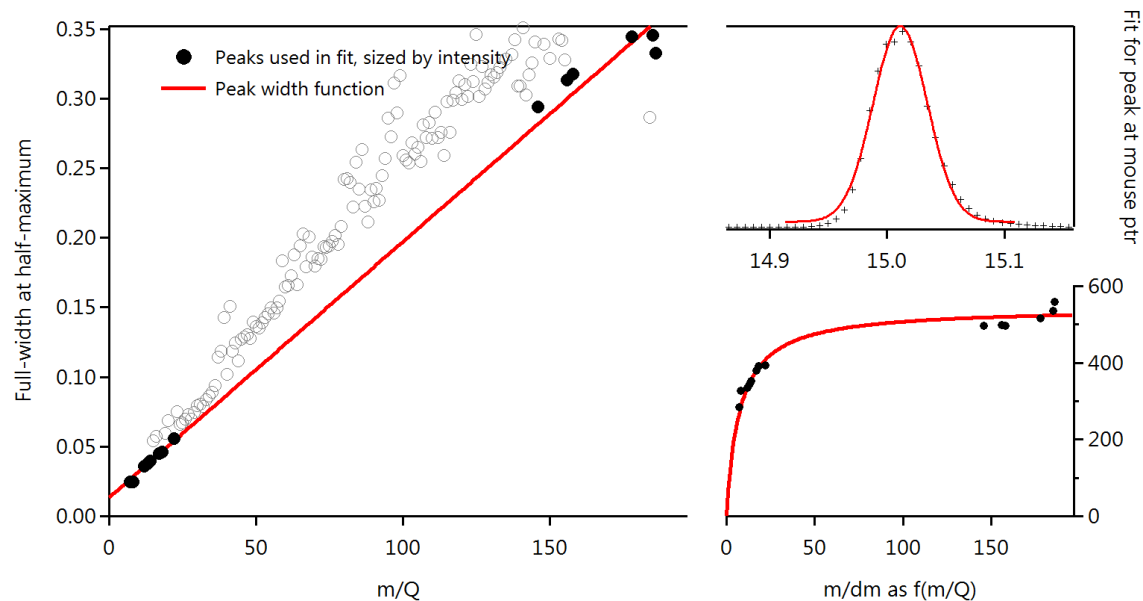
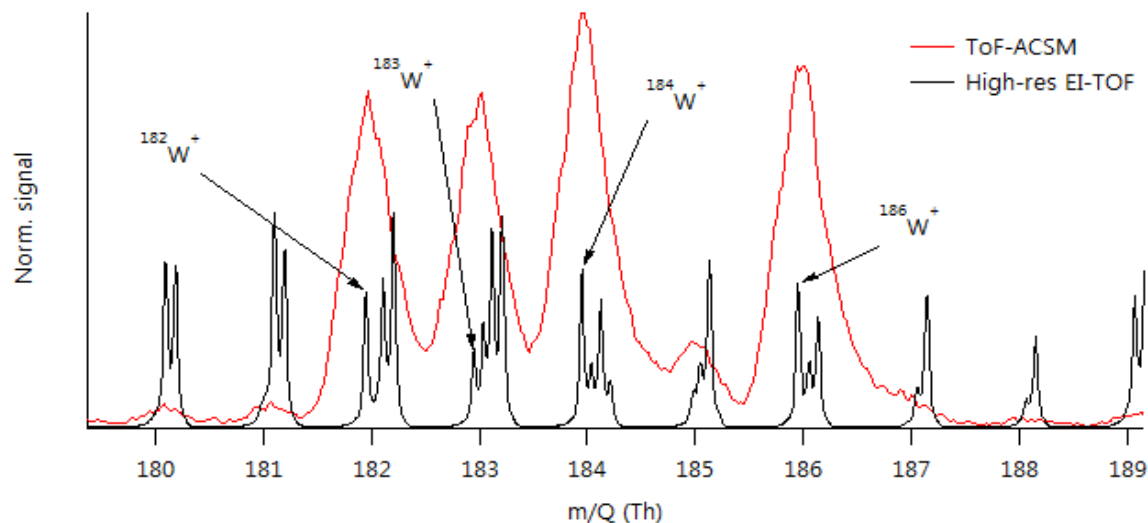
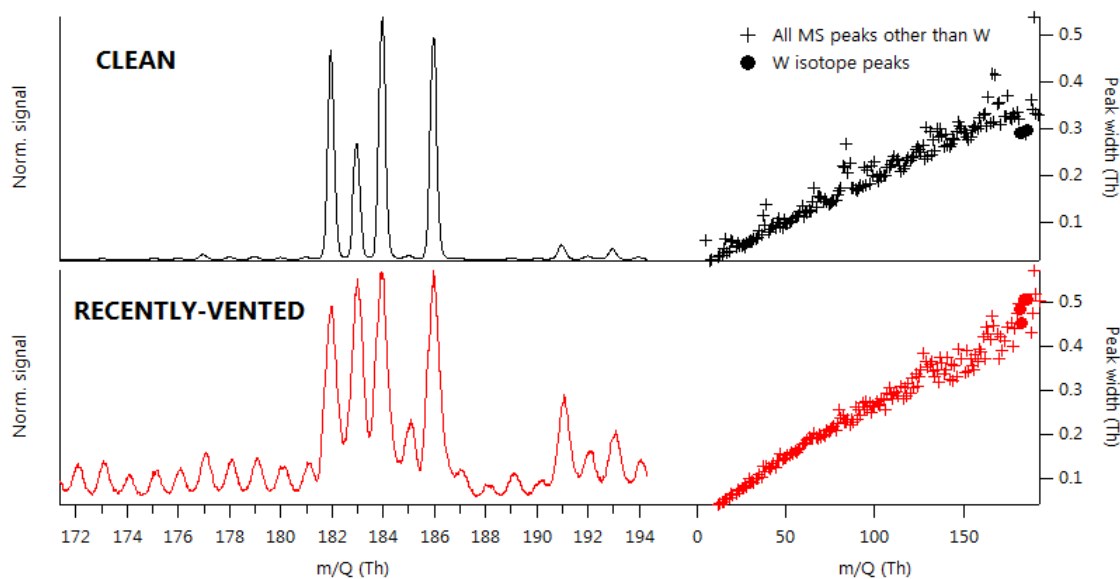


Figure 2: Ascertaining the peak width as a function of  $m/Q$ : the straight-line fit (peak width function, in red) is applied to the chosen data points (in black), giving the relationship for mass resolving power shown bottom-right. The principle behind this methodology is that isolated ions (in black) should exhibit narrower peak widths than those with adjacent ions (in grey).

10



**Figure 3:** Comparison of a high-resolution EI-TOF MS with that from the ToF-ACSMS. Note that the ToF-ACSMS tungsten peaks are much stronger relative to the background than is observed in the EI-TOF. The multiple ions visible in the EI-TOF are measured as only single, broad, peaks in the ToF-ACSMS.



**Figure 4:** Left, example ToF-ACSMS mass spectra for clean and recently-vented (ie, dirty) vacuum chambers, showing the tungsten isotope ion pattern superimposed on background peaks of different relative magnitudes. Right, width of the isobaric peaks as a function of mass-to-charge for the same MS. The solid circles denote the isobars containing the tungsten isotope peaks. These lie under the general trend in the clean case, but follow the trend in the recently-vented case. Owing to instrument tuning, the peaks are generally broader in the recently-vented case.

5

10

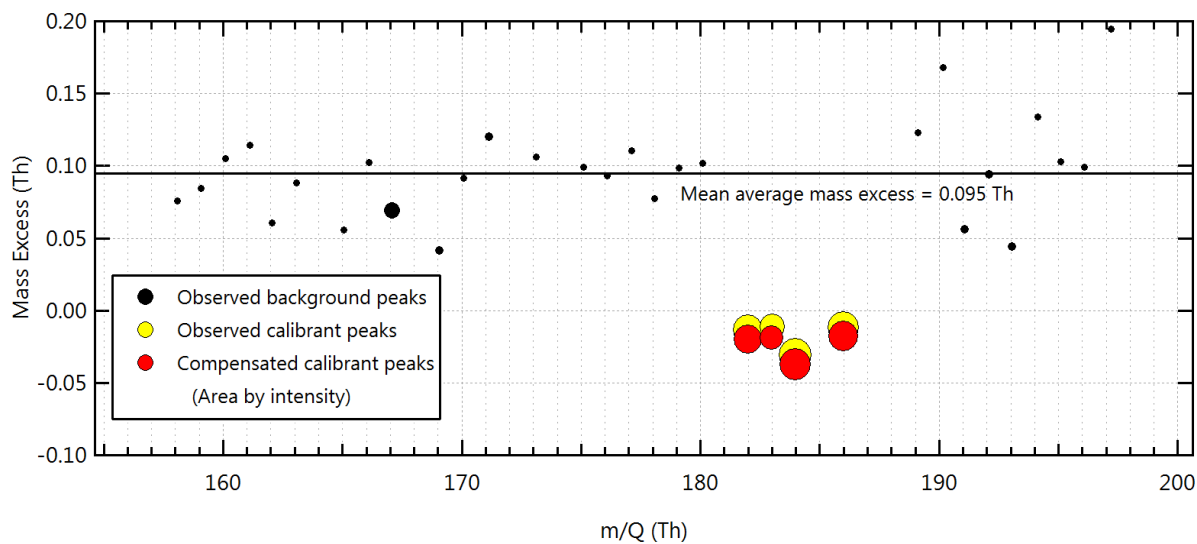


**Figure 5:** Compensating for the mass positions of calibrant peaks by assuming interferences are present of equal magnitude and mass excess to the surrounding isobaric peaks.

5

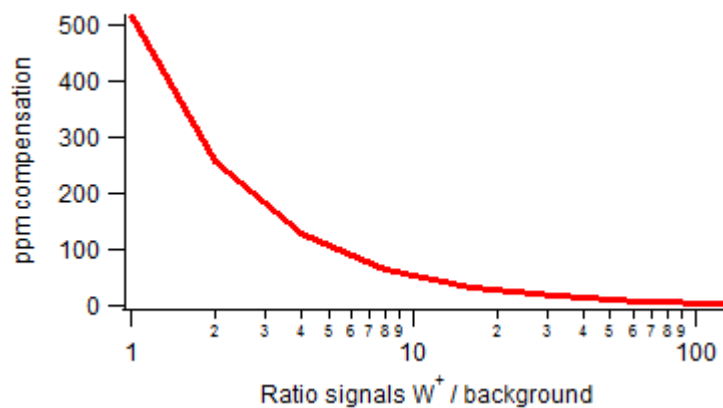


**Figure 6:** Estimated relative compensation that would need to be applied to the  $W^+$  exact mass owing to an influencing, overlapping, background peak separated by 0.095 Th and of relative signal strength indicated by the x-axis.

10

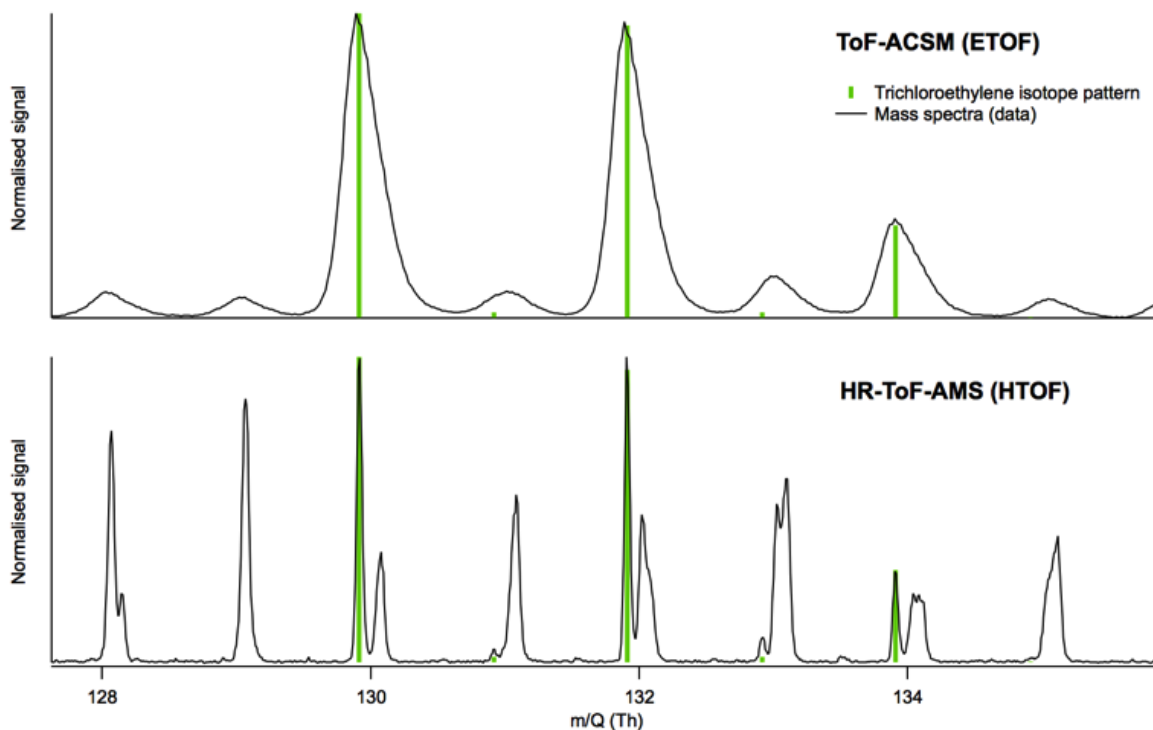
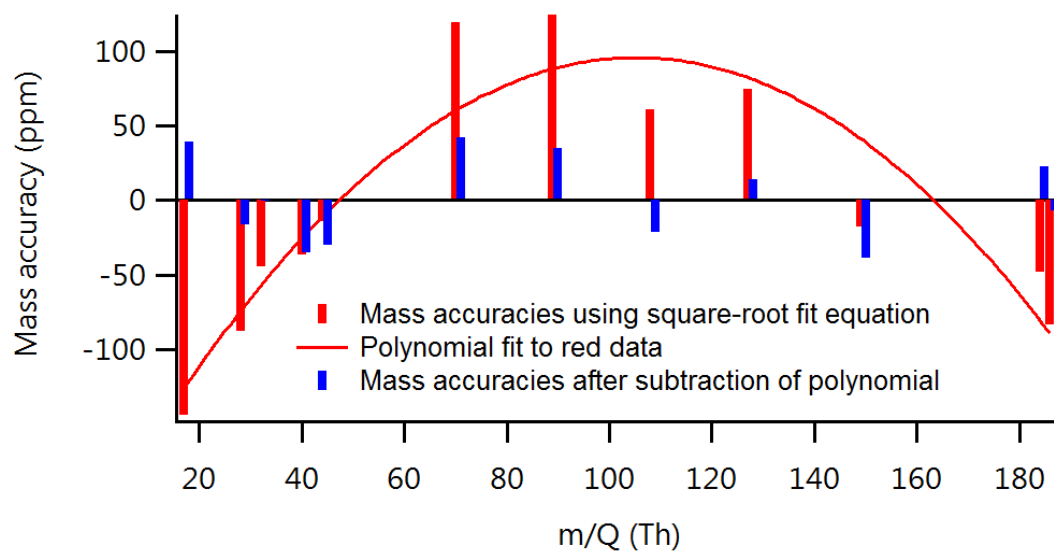


**Figure 7:** Mass spectra from the ToF-ACSM and HR-ToF-AMS showing the isotope pattern of trichloroethylene ( $C_2Cl_3H^+$ ).



5 **Figure 8:** Fitting mass calibration fit residuals with a polynomial

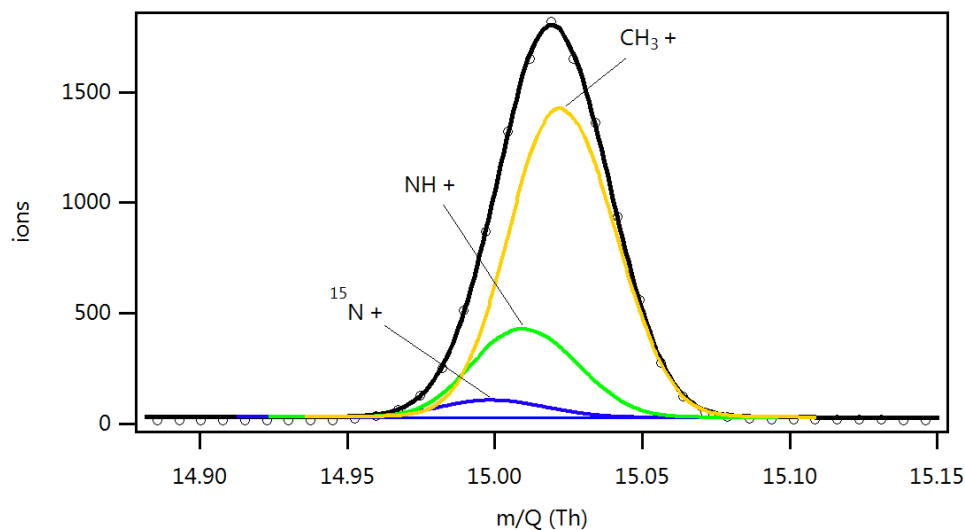


**Figure 9:** The isobaric peaks  $^{15}\text{N}^+$  ( $m/Q = 14.9996$  Th),  $\text{NH}^+$  ( $m/Q = 15.01035$  Th) and  $\text{CH}_3^+$  ( $m/Q = 15.0229$  Th) at 15 Th have peak separations of 0.5 half-widths for mass resolving power  $m/\Delta m = 300$ .

5

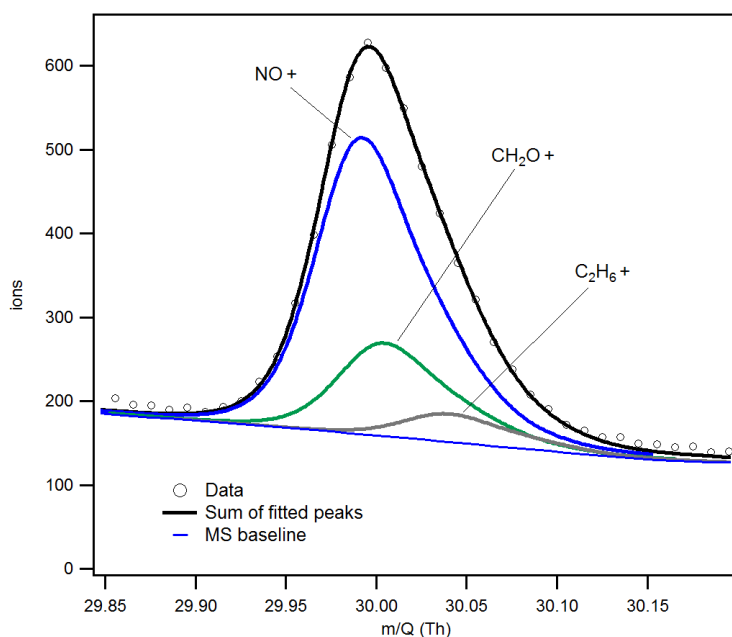


**Figure 10:** The isobaric peaks from  $\text{NO}^+$  ( $m/Q = 29.997$  Th) and  $\text{CH}_2\text{O}^+$  ( $m/Q = 30.010$  Th) at 30 Th have a peak separation of 0.34 half-widths for resolving power  $m/\Delta m = 400$ .

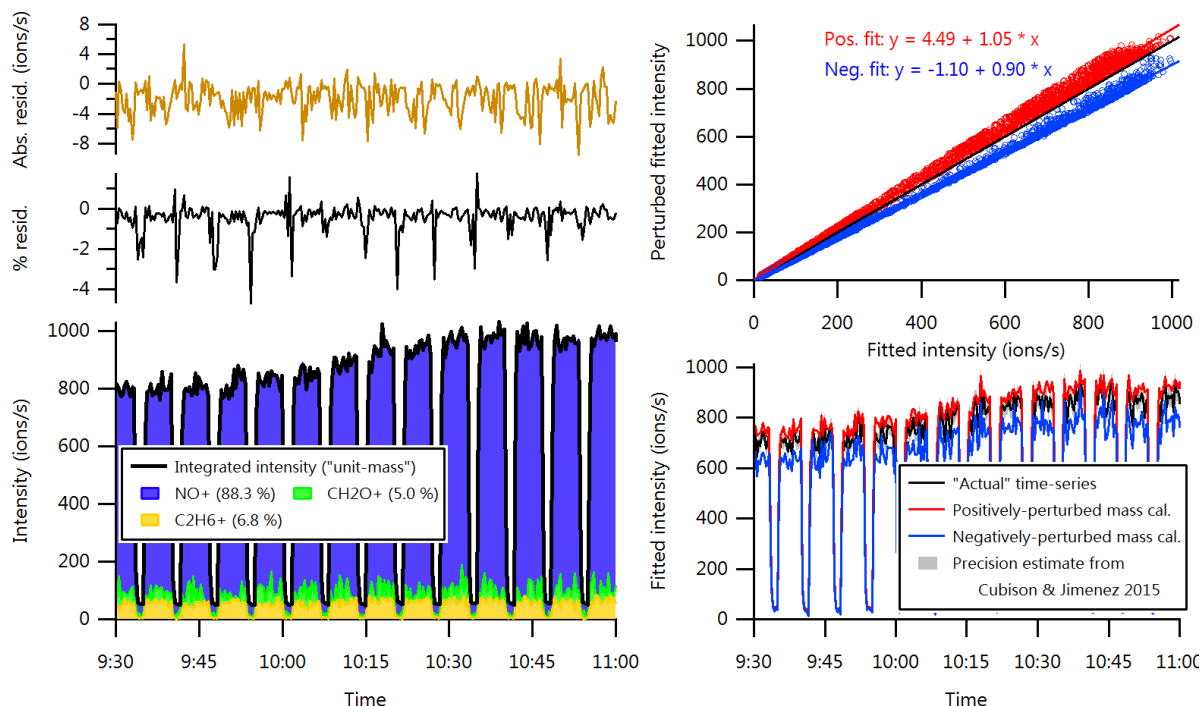


**Figure 11:** Assessing the sensitivity of the fitted peak intensity of the  $\text{NO}^+$  ion to perturbations in the mass calibration of  $\pm 20$  ppm. Left: the sum of the ions fitted at this peak compared with the integrated signal (bottom) and the absolute and relative residuals (top). Top right: Scatter plots of the fitted  $\text{NO}^+$  signals for the perturbed vs best-case mass calibration scenarios. Bottom right: Time-series of the fitted  $\text{NO}^+$  intensities, with the perturbed mass calibration cases shown in red and blue. The shading around the black line indicates the expected precision predicted by the parameterisation of Cubison and Jimenez (2015).

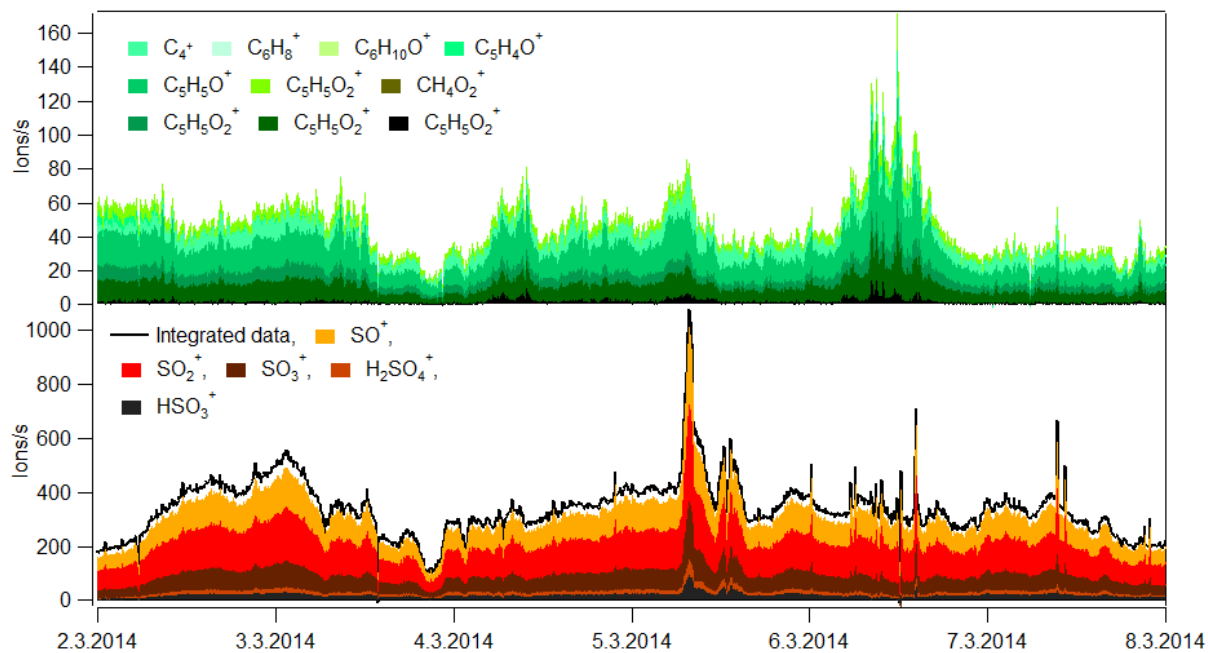


**Figure 12:** Concentrations of main sulphate ions ( $\text{SO}^+$ ,  $\text{SO}_2^+$ ,  $\text{SO}_3^+$ ,  $\text{HSO}_3^+$  and  $\text{H}_2\text{SO}_4^+$ ) from peak fitting and sulphate calculated from application of the fragmentation table with integrated data (lower panel) and timeseries of the isobaric organic ions in the same m/Q as sulphate fragments (upper panel).

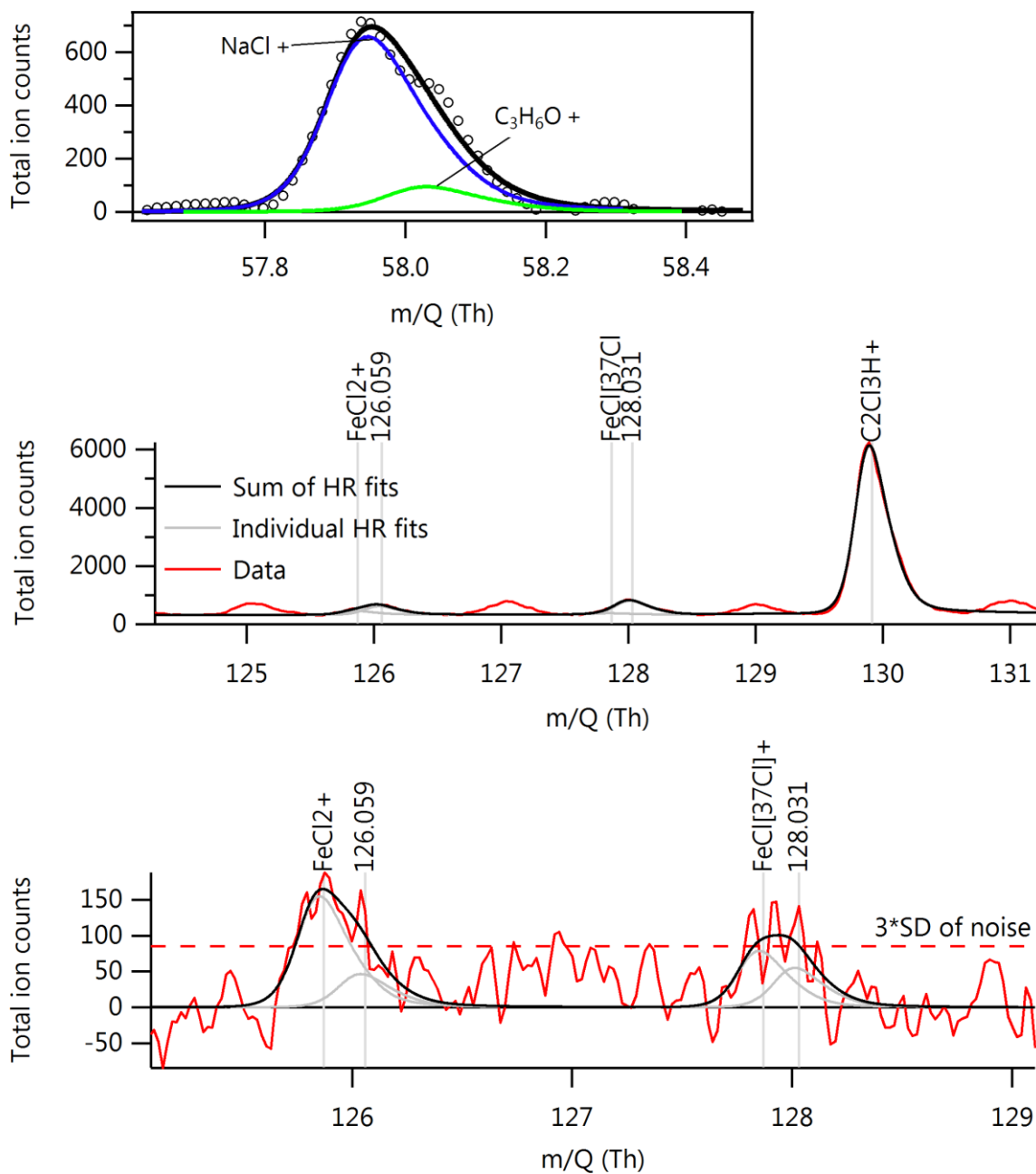


**Figure 13:** Top: Isobaric peaks of  $\text{NaCl}^+$  and  $\text{C}_3\text{H}_6\text{O}^+$ . Centre: Total mass spectrum showing the calibrant ion  $\text{C}_2\text{Cl}_3\text{H}^+$  and signals from unknown compounds at nominal masses 126 and 128 Th. Bottom: Difference mass spectrum (ambient minus filter) showing statistically-relevant signals from the isotopes  $\text{Fe}^{35}\text{Cl}_2^+$  and  $\text{Fe}^{37}\text{Cl}^{35}\text{Cl}^+$ .

5

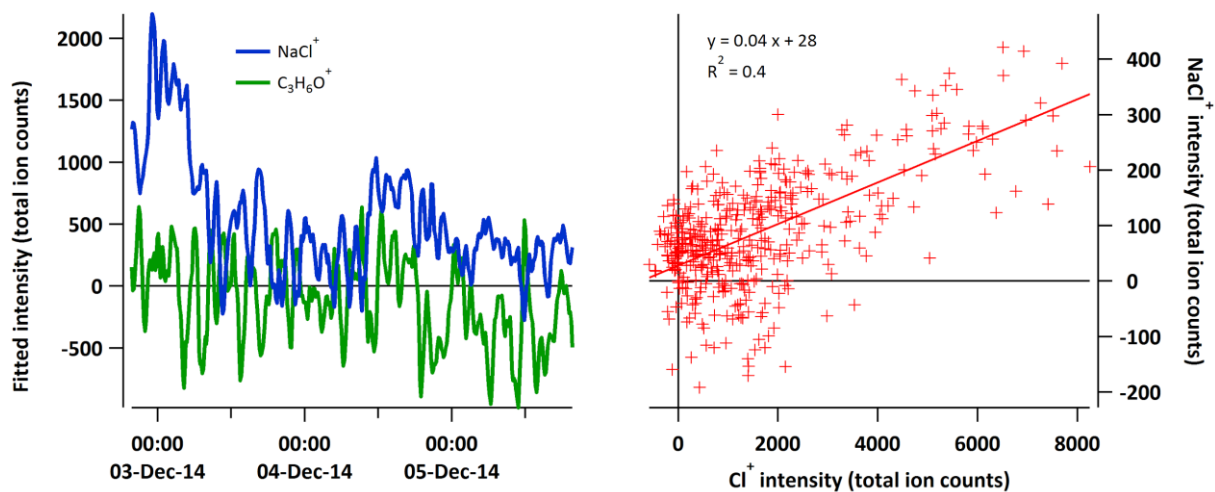


**Figure 14:** Left: time-series (1-hr integration period) of the fitted intensities for the isobaric ions  $\text{NaCl}^+$  ( $m/Q = 57.96$  Th) and  $\text{C}_3\text{H}_6\text{O}^+$  ( $m/Q = 58.04$  Th). Right: correlation of the  $\text{NaCl}^+$  ion signal with that of  $\text{Cl}^+$  (10-min integration period).

5

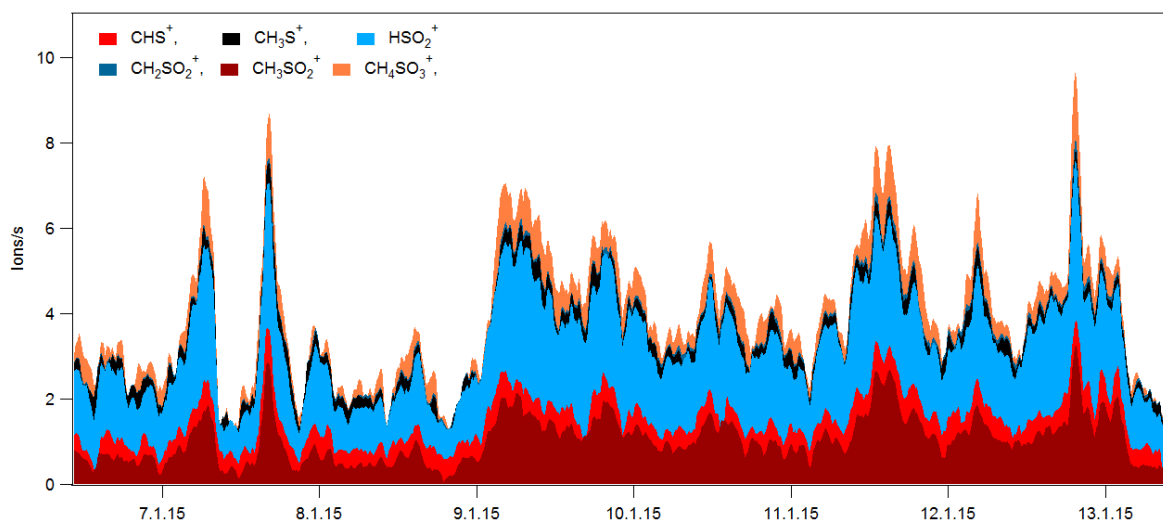


**Figure 15:** Timeseries of MSA fragments  $\text{CHS}^+$  (44.98 Th),  $\text{CH}_3\text{S}^+$  (47.00 Th),  $\text{HSO}_2^+$  (64.97 Th),  $\text{CH}_2\text{SO}_2^+$  (77.98 Th),  $\text{CH}_3\text{SO}_2^+$  (78.99 Th) and  $\text{CH}_4\text{SO}_3^+$  (95.99 Th) during episode 2.

10

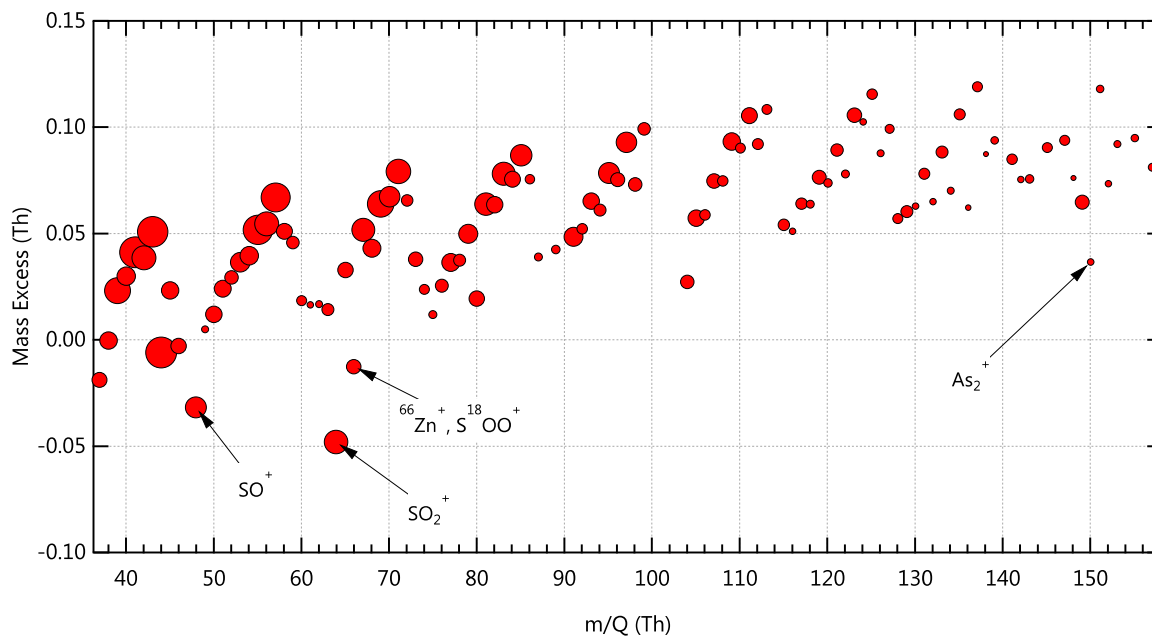
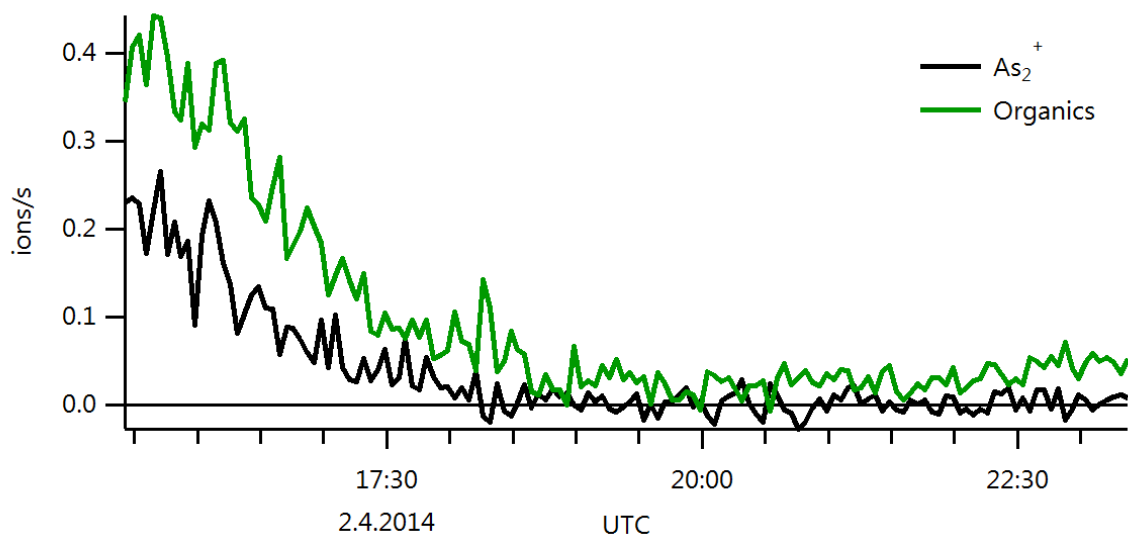
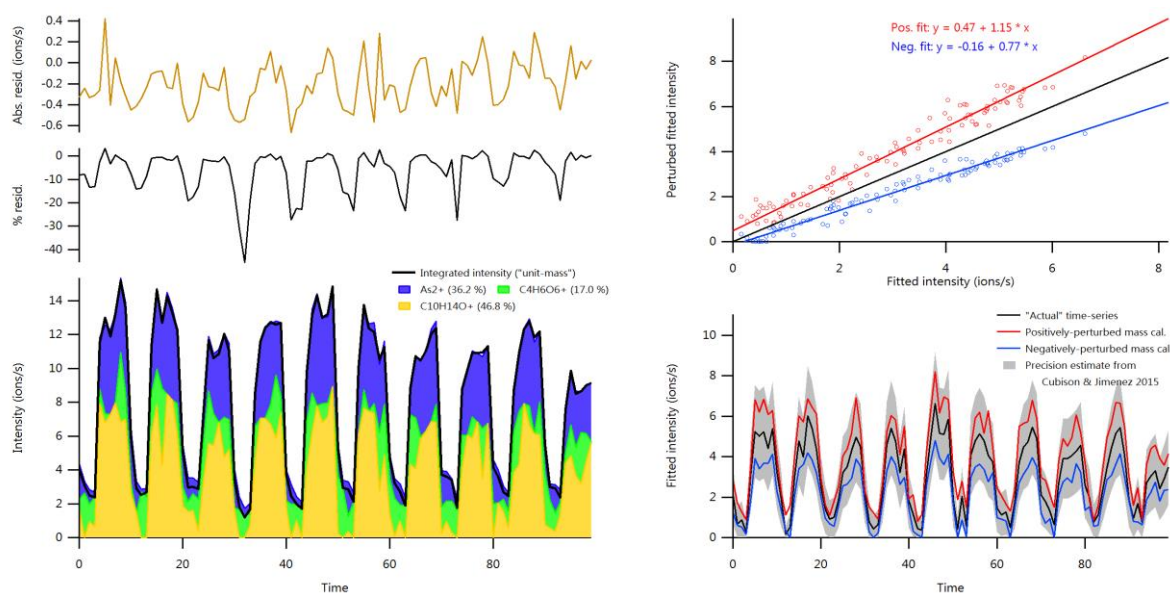


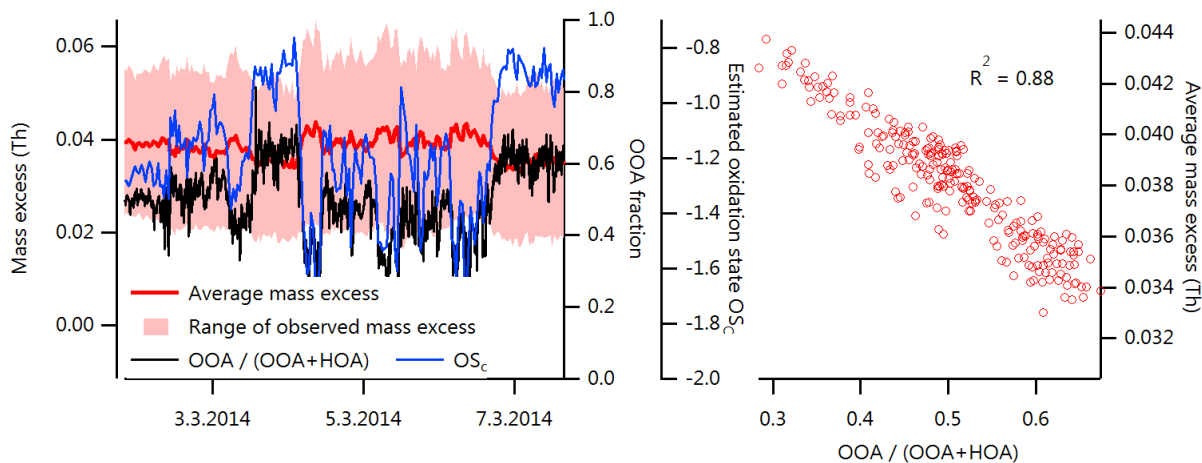
**Figure 16:** Mass excess plot for the isobaric peaks visible in a MS from the underground min data. The peaks containing the Arsenic and  $\text{SO}_x$  ions are indicated. The data points are sized according to the log of the peak intensity.



5 **Figure 17:** Time series of the mass loadings calculated from peak-fitting for the isobaric peaks at 150 Th. The organics trace represents the sum of the signals from the peaks  $\text{C}_4\text{H}_6\text{O}_6^+$  and  $\text{C}_{10}\text{H}_{14}\text{O}^+$ .



5 **Figure18:** Assessing the sensitivity of the fitted peak intensity of the  $As_2^+$  ion to perturbations in the mass calibration of +/- 200 ppm. Left: the sum of the ions fitted at this peak compared with the integrated signal (bottom) and the absolute and relative residuals (top). Top right: Scatter plots of the fitted  $As_2^+$  signals for the perturbed vs best-case mass calibration scenarios. Bottom right: Time-series of the fitted  $As_2^+$  intensities, with the perturbed mass calibration cases shown in red and blue. The shading around the black line indicates the expected precision predicted by the parameterisation of Cubison and Jimenez (2015).



10 **Figure 19:** Time-series (left) and regression (right) of the average mass excess and OOA fractions. Shown also the time-series of the estimated carbon oxidation state from mass excess analysis.

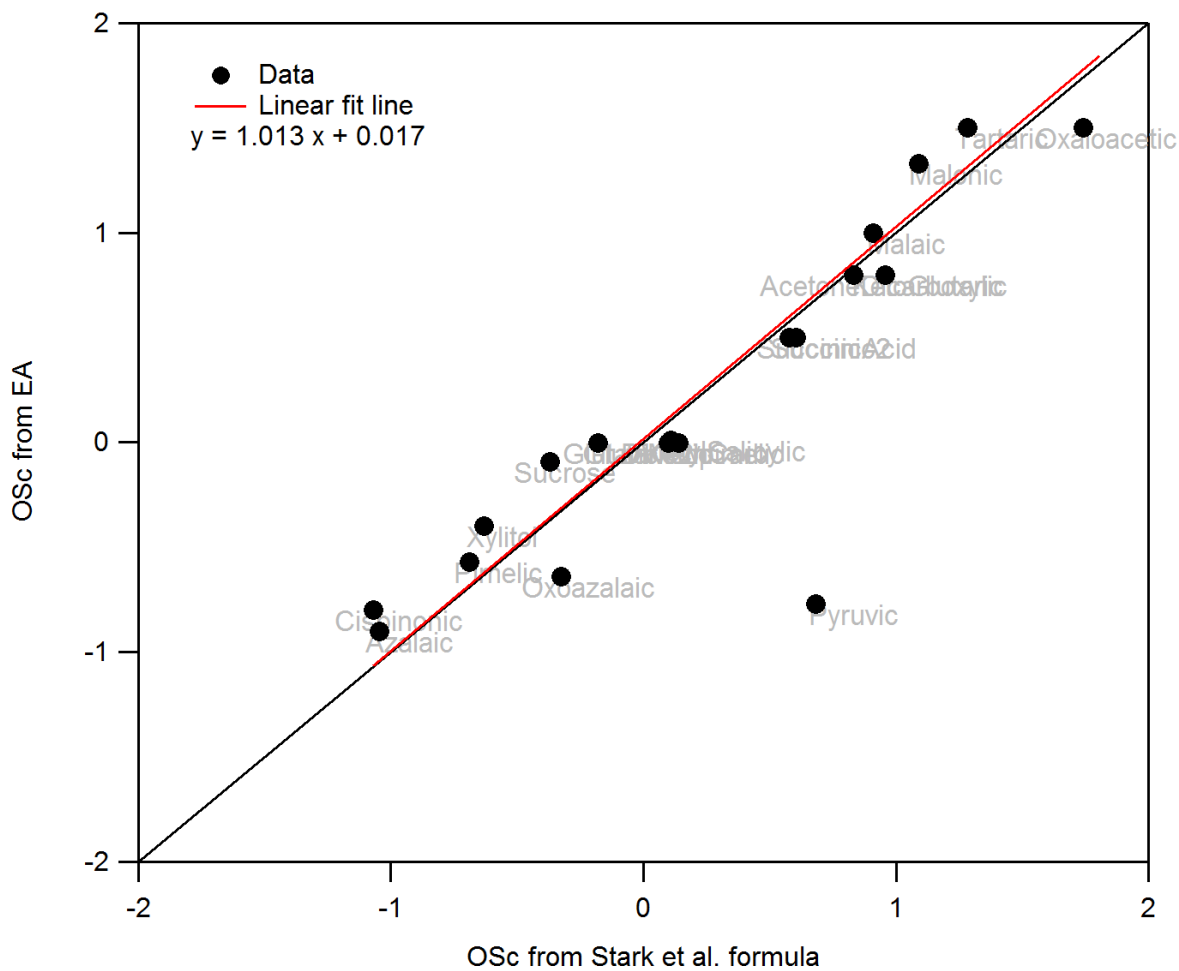


**Figure 20:** Carbon oxidation state of various organic compounds calculated from elemental analysis compared to the estimates using the Stark et al. formula.